UNIVERSIDADE FEDERAL DO RIO GRANDE DO SUL
GRADUATE PROGRAM IN PHYSICS
Thesis

Metal oxides of resistive memories investigated by electron and ion backscattering

Gabriel Guterres Marmitt

Brazil
October, 2017

Gabriel Guterres Marmitt

Metal oxides of resistive memories investigated by electron and ion backscattering

Thesis prepared under the supervision of Prof. Pedro Luis Grande, co-supervision of Prof. Maarten Vos and presented to the Institute of Physics at UFRGS in partial fulfillment of the requirements for obtaining the title of Doctor in Physics.

Universidade Federal do Rio Grande do Sul – UFRGS

Instituto de Física

Programa de Pós-Graduação

Supervisor: Pedro Luis Grande

Co-supervisor: Maarten Vos

Brazil

October, 2017

Gabriel Guterres Marmitt Metal oxides of resistive memories investigated by electron and ion backscattering/ Gabriel Guterres Marmitt. – Brazil, October, 2017-
72 p. : il. (color) ; 30 cm.

Supervisor: Pedro Luis Grande
Co-supervisor: Maarten Vos

Thesis (PhD) – Universidade Federal do Rio Grande do Sul – UFRGS
Instituto de Física
Programa de Pós-Graduação, October, 2017.

1. RRAM devices. 2. Electron RBS. 3. Oxygen self-diffusion.

In memory of Masahiro Hatori

"Do not go gentle into that good night.
Rage, rage against the dying of the light.
— Dylan Thomas

Agradecimentos

Primeiramente gostaria de agradecer ao Prof. Pedro, mais do que simples orientador tu és um grande amigo e mentor. Tive o privilégio de aprender e crescer contigo, e por isso serei eternamente grato. Ao Prof. Maarten Vos pela paciência e disposição que teve comigo durante minha estadia na ANU.

À minha esposa Vivian, pelo amor e compreenção que teve durante estes anos. Este doutorado, e minha felicidade, não seriam possíveis sem você ao meu lado. Como um quadrúpede chegamos mais longe.

Aos meus pais, José Carlos e Edith, pelo apoio incondicional que sempre recebi.

À colega Milena Sulzbach, pelas horas de discussão e ajuda com os experimentos.

Aos colegas Henrique e Igor, pela mais honesta amizade. Sou grato pelas ótimas conversas e, claro, pelas cervejas. Xablau!

Abstract

MARMITT, G. G. **Metal oxides of resistive memories investigated by electron and ion backscattering**

The memristor is one of the most promising devices being studied for multiple uses in future electronic systems, with applications ranging from nonvolatile memories to artificial neural networks. Its working is based on the forming and rupturing of nano-scaled conductive filaments, which drastically alters the device's resistance. These filaments are formed by oxygen vacancy accumulation, hence a deep understanding of the self-diffusion of oxygen in these systems is necessary. Accurate measurements of oxygen self-diffusion on metal oxides was achieved with the development of a quantitative analysis of the energy spectrum of the backscattering of electrons. The novel technique called Electron Rutherford Backscattering Spectroscopy (ERBS) uses the scattering of high energy electrons ($\approx$ 40 keV) to probe the sample's near surface (10–100 nm). Measurements of the high energy loss region – called Reflection High-Energy Electron Loss Spectroscopy (RHEELS) – also exhibit characteristics of the material's electronic structure. A careful procedure was developed for the fitting of ERBS spectra, which was then applied on the analysis of multi-layered samples of Si_3N_4/TiO_2, and measurements of the band gap of common oxides, such as SiO_2, $CaCO_3$ and Li_2CO_3. Monte Carlo simulations were employed to study the effects of multiple elastic scatterings in ERBS spectra, and a dielectric function description of inelastic scatterings extended the simulation to also consider the plasmon excitation peaks observed in RHEELS. These analysis tools were integrated into a package named PowerInteraction. With its use, a series of measurements of oxygen self-diffusion in TiO_2 were conducted. The samples were composed of two sputtered deposited TiO_2 layers, one of which was enriched with the 18 mass oxygen isotope. After thermal annealing, diffusion profiles were obtained by tracking the relative concentration of oxygen isotopes in both films. From the logarithmic temperature dependence of the diffusion coefficients, an activation energy of $\approx$ 1.05 eV for oxygen self-diffusion in TiO_2 was obtained. Common ion beam analysis, such as RBS and NRA/NRP (Nuclear Reaction Analysis/Profiling), were also used to provide complementary information.

Resumo

MARMITT, G. G. **Óxidos metálicos de memórias resistivas investigados por retroespalhamento de elétrons e íons**

O *memristor* é um dos dispositivos mais promissores sendo estudados para múltiplos usos em sistemas eletrônicos, com aplicações desde memórias não voláteis a redes neurais artificiais. Seu funcionamento é baseado na formação e ruptura de filamentos condutores nanométricos, o que altera drasticamente a resistência do dispositivo. Estes filamentos são formados pela acumulação de vacâncias de oxigênio, portanto um profundo entendimento da autodifusão de oxigênio nestes sistemas é necessário. Medidas acuradas da difusão em óxidos metálicos foi obtida com o desenvolvimento de uma análise quantitativa do espectro em energia de elétrons retroespalhados. A inovadora técnica de RBS de elétrons (ERBS) utiliza elétrons de alta energia ($\approx$ 40 keV) para investigar a região próxima a superfície (10–100 nm). Medidas da região de alta perda de energia – chamada de Spectroscopia de Perda de Alta-Energia de Elétrons Refletidos (RHEELS) – também exibe características da estrutura eletrônica dos materiais. Um procedimento cuidadoso para o ajuste de espectros de ERBS foi desenvolvido, e então aplicado na análise de amostras multi camada de Si_3N_4/TiO_2, e medidas de band gap de alguns óxidos, como SiO_2, $CaCO_3$ e Li_2CO_3. Simulações de Monte Carlo foram empregadas no estudo dos efeitos de espalhamento múltiplo nos espectros de ERBS, e uma descrição dielétrica dos espalhamentos inelásticos extendeu as simulação para também considerarem os picos de exitação plasmônica observados em RHEELS. Estas ferramentas de análise foram integradas em um pacote chamado PowerInteraction. Com o uso deste, uma série de medidas de autodifusão de oxigênio em TiO_2 foram conduzidas. As amostras eram compostas por dois filmes de TiO_2 depositados por *sputtering*, um dos quais enriquecido com isótopo 18 de oxigênio. Após tratamentos térmicos, perfis de difusão foram obtidos pelo rastreio das concentrações relativas dos isótopos de oxigênio nos dois filmes. Do comportamento logarítmico dos coeficientes de difusão em relação à temperatura, uma energia de ativação de $\approx$ 1.05 eV para a autodifusão de oxigênio em TiO_2 foi obtida. Análises por feixes de íons, como RBS e NRA/NRP (Análise/Perfilometria por Reação Nuclear), também forneceram informações complementares.

List of Figures

List of abbreviations and acronyms

ALD	Atomic Layer-Deposition
ANU	Australian National University
CF	Conductive Filament
CMOS	Complementary Metal-Oxide Semiconductor
CNPq	Conselho Nacional de Desenvolvimento Científico e Tecnológico
DCS	Differential Cross Section
EME	Electronic Materials Engineering
ERBS	Electron Rutherford Backscattering Spectrometry
FBA	First Born Approximation
HP	Hewlett Packard
IBA	Ion Beam Analysis
IMFP	Inelastic Mean Free Path
MEIS	Medium Energy Ion Spectrometry
NRA	Nuclear Reaction Analysis
NRP	Nuclear Reaction Profiling
OV	Oxygen Vacancy
PECVD	Plasma-enhanced Chemical Vapor Deposition
RBS	Rutherford Backscattering Spectrometry
RHEELS	Reflection High-Energy Electron Loss Spectroscopy
RRAM	Resistive Random-Access Memory
SATP	Standard Ambient Temperature and Pressure
SIMS	Second Ion Mass Spectroscopy
XPS	X-ray photoelectron spectroscopy

Contents

1 Introduction

The *memristor* is currently highlighted as one of the most promising devices being studied for multiple uses in nano-electronic systems. High device integration density, low power consumption, high data and endurance retention, fast switching speed, and most importantly CMOS (Complementary Metal-Oxide Semiconductor) compatibility are some the best performance features which have been demonstrated in published experimental results of memristors prototypes. This combination of many advantageous characteristics in a single device certainly justifies the great research interest that devices based on *resistive switching* have attracted over the last few years. This attention is also justified by the existing rumors about its imminent use in both storage and processing units of future electronic systems.

In 2008, Hewlett Packard (HP) researchers unveiled the exciting discovery of nonvolatile memristive behavior in Titanium dioxide (TiO_2)-based nano-films (1). Since then both academia and industry have actively searched for new memristive materials and large scale manufacturing technologies. Based on two thin-layer TiO_2 films, the HP's device remains up to now the most generally recognized memristor type. Its functioning depends on oxygen vacancy drift and diffusion; depletion of oxygen causes the crystal to rearrange, which affects its resistivity. The bottom layer acts as an insulator whereas the top film layer acts as a conductor via oxygen vacancies in the TiO_2. The application of an electrical field causes oxygen vacancies to move from the top layer towards the bottom layer, forming a *conductive filament* (CF) in the process. Complex dynamics on the nano-scale are involved in the resistive switching process, for this reason great effort has been devoted to the development of physical models to describe these systems. An appropriate model, not only leads to a better understand of its behavior, but also results in a better exploitation of its unique properties in novel systems and architectures combining data storage and data processing in the same physical location.

With an unique combination of superior properties, an array of promising applications have been inspired by memristors technology. These include uses in nonvolatile memory (2, 3, 4, 5, 6, 7, 8), artificial neural networks (9, 10), chaotic circuits (11, 12), programmable logic devices (13, 14, 15), and signal processing and pattern recognition circuits (16). Simulations considering some of the nonvolatile memories and neuromorphic applications (17) showcase the impact the technology has had, as both these applications are currently in profound demand. Memristor-based nonvolatile memory, such as Resistive RAMs, seems to be the only solution in the age of big data while a completely new paradigm of brain inspired computing is currently been explored via neuromorphic devices (6).

Accordingly, to realize this technological potential, experimental measurements of the resistive switching operation has become a field of intense research. However, due to the limited contrast between the CF and its environment and because these phenomena occur at virtually inaccessible lengths scales, characterizations have required formidable experimental effort (18, 19, 20), limiting physical understanding. Transmission electron microscopy is the de facto characterization technique, yet it typically provides only a single filament state snapshot. This difficulty in direct measuring the filament formation and rupturing inspired the scientific community to make experimental efforts on the understanding of physical mechanisms which govern memristive switching.

Figure 1 – The memristor

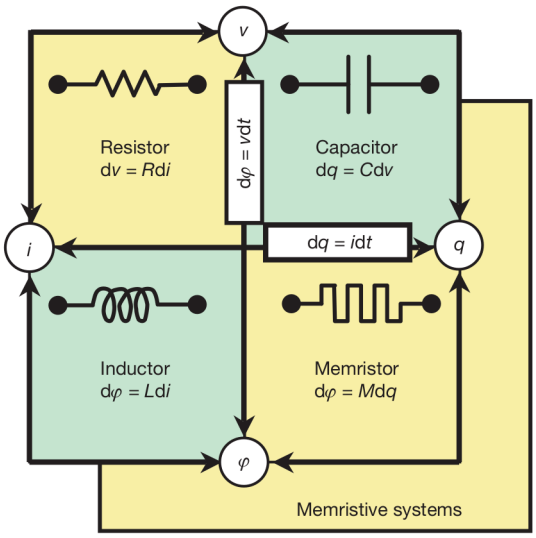

Source: Strukov et al.(1) 2008.

Physical models reveal that the CF is ruptured and formed locally inside the switching layer. The *set* process involves field and thermal-driven filament formation followed by filament expansion, while the *reset* process is dominated by thermal-driven filament rupture followed by gap widening. The competition between drift and diffusion components during *reset* can lead to different resistive switching characteristics. Hence, studies of oxygen diffusion aid the understanding of CFs behavior during *set* and *reset* processes, and could contribute to the understanding of the complicated subject of resistive switching.

Several phenomena in nanomaterial science depend on some form of diffusion or ion migration with or without the presence of an electrical field. Examples include the synthesis, oxidation, phase transitions and crystals growth. Many thermodynamic properties are influenced by diffusion, or its absence. Therefore, the self-diffusion of oxygen is an important process, but difficulties in its study are evident. Even for silicon, probably the most studied material, the topic of self-diffusion is still actively researched (21). The few techniques that can measure self-diffusion, rely on the presence of rare or radioactive isotopes. The analysis is typically performed with SIMS (Second Ion Mass Spectroscopy) or some ion beam technique, such as NRA/NRP (Nuclear Reaction Analysis/Profiling), RBS (Rutherford Backscattering Spectrometry) or MEIS (Medium Energy Ion Spectrometry).

The diffusion in TiO_2 is particularly interesting, being one of the the best candidates for the fabrication of RRAMs based on resistive switching. Substoichiometric CFs are formed due to oxygen vacancy accumulation and are responsible for the enhanced

conductivity. The diffusion is quite complicated in these systems due to the different charge states possible, for both the vacancies and the oxygen interstitials. Moreover, crystallization and grain boundaries could have an effect on the diffusion.

The measurement of diffusion in titania films with thicknesses on the order of 10's of nm makes necessary to resolve small diffusion lengths of 1–10nm. Common ion beam techniques are capable of high spatial resolution but require special care to avoid undesirable damage caused by the ion bombardment, which could contribute to the measured diffusion. In this regard, the use of the less destructive ERBS technique was demonstrated for oxygen self-diffusion measurements in HfO_2 (22), in which isotopic marking was used to detect the diffusion profiles. The experiment was possible due to ERBS great mass resolution that made it possible to measure the 16 and 18 oxygen isotopes separately.

Related to the ion beam technique of RBS, Electron RBS (ERBS) utilizes the scattering of high energy electrons ($\approx$ 40 keV) to probe the sample's near surface (10–100 nm). Additionally, measurements of the high energy loss region – also called Reflection High-Energy Electron Loss Spectroscopy (RHEELS) – exhibit characteristics of the electronic structure, similar to XPS (X-ray Photoelectric Spectroscopy) measurements. The result is a feature-rich energy loss spectrum, for which analysis via a careful fitting procedure can simultaneously obtain information about atomic, chemical and electrical properties of the material.

During this project I have stayed for six months in Canberra–Australia at the Atomic and Molecular Physics Laboratories (AMPL) department of the Australian National University (ANU) under supervision of Prof. Dr. Maarten Vos. A PhD. exchange program known as *Ciência sem Fronteiras*, which was kindly granted by *Conselho Nacional de Desenvolvimento Científico e Tecnológico* (CNPq), allowed me to conduct measurements with the unique ERBS technique. The system was build mainly by Went and Vos, which have published numerous articles describing its functioning in detail (23, 24, 25).

Besides the experimental program reported here, a simulation software called PowerMEIS was developed. As its name suggest, it has roots in MEIS spectra simulations, but as the used techniques became more diverse so did the software. A comprehensive description of its last version, called PowerInteraction, is given on Appendix A, which also covers its worldwide availability as an online service.

Objectives

The main objective is the characterization of metallic oxides, with particular interest in measurements of physical properties connected to the resistive switching process occurring in resistive memories, such as oxygen self-diffusion and band gap values. In

order achieve accurate measurements, the development of better quantitative analyses for backscattering of ions and electrons are necessary. For this end, both analytical calculations and computational simulations should be explored. Special attention will be given to non-destructive techniques, such as the ERBS.

Work outline

This Thesis is organized as follow: Section 1.1 briefly reviews the current RRAM technology, introducing the importance of TiO_2 in its development and the fundamental relation between diffusion and the resistive switching phenomenon. Section 1.2 covers the experimental setting used in ERBS experiments and describes the physical principles behind the technique. Chapter 2 describe ERBS analysis improvements on multi-layer fittings. Chapter 3 extends the fitting to consider the band gap onset in the energy-loss spectrum. Chapter 4 discusses the development of a Monte Carlo algorithm for simulations of electron interactions with matter. Chapter 5 presents a set of oxygen self-diffusion measurements in TiO_2. Chapter 6 summarizes the conclusions reached during the progress of this research.

1.1 Resistive RAMs

Resistive Random Access Memories (RRAMs) are devices that operate in two states with distinct resistivities to store and process binary information. The *on*-state is achieved by the formation of CFs during a *set* process, which results in the device transitioning from a high to a low resistance state. The rupture of the CF through a *reset* process leads to the opposite *off*-state. Except for some cases, such as ternary oxides that present changes in resistivity due to interface effects (26, 27), the majority of metallic oxides are known to have CFs as the primary mechanism to switch the device resistance (28, 29, 20, 30, 31). Filament switching was demonstrated in unipolar (*set* and *reset* are performed using positive voltages (32, 33, 29, 31)) and bipolar (positive/negative voltages used during *set*/*reset*, or vice-versa) methods, which sometimes coexist in some materials (34, 35, 36).

These devices are attracting great interest for their use in new technologies involving dynamic memories. However, to successfully develop RRAM technology many problems still need to be solved, including the switching mechanism (37, 38, 39), reduction in the *reset* current (32, 33, 40) and reliability (41, 42, 43).

The text is laid out as follows: first, a general classification of RRAM is given (Subsec. 1.1.1); next, the importance of TiO_2 as an insulator layer in RRAM technology is discussed (Subsec. 1.1.2) and then a simple mathematical switching model is presented (Subsec. 1.1.3).

1.1.1 Classification of RRAM devices

RRAM devices may be classified based on some of the I-V characteristics during the *set* and *reset* processes. In unipolar devices, showed on Fig. 2 a, both the *set* and *reset* can be achieved by applying either positive or negative voltage. Henceforth, there is no polarity dependence of the I-V characteristics in these systems. For such devices, a current compliance has to be applied during the *set* to avoid excessive heat generation, which could destroy the CFs soon after formation. In contrast, during *reset* a large current is intentionally generated to break the CFs, causing the device to switch back to a high resistance *off*-state. Therefore, the *set* compliance current is generally much smaller than the *reset* rupture current.

In bipolar RRAM devices, a stable *set* is only possible when a positive voltage is applied across the device (see Fig. 2 b). Moreover, the *reset* process needs a voltage that is always opposite to that used during *set*. For this case, the *reset* is only achievable when the voltage is negative, thus defining the device as a bipolar RRAM. In general, bipolar devices are more power efficient and employ much smaller *reset* currents than unipolar devices. For this reason, the study described here is focused on bipolar devices.

Figure 2 – *Uni* and *Bi* - Polar RRAM characteristics

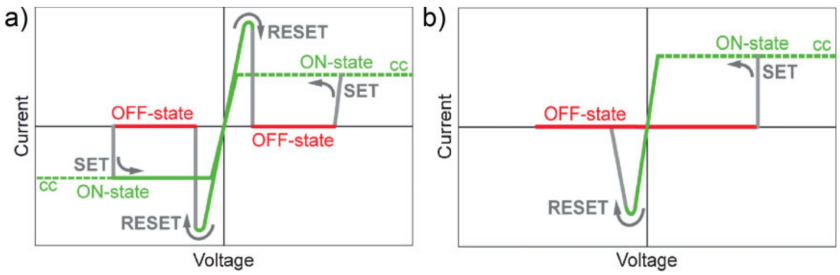

Source: Waser et al.(44) 2009.

A different classification is based on operation principles and device physics. From this point of view, the two main types of devices are known as Electrochemical Metallization (ECM) RRAMs and Oxygen Vacancies based (OV-based) RRAMs. In ECM RRAMs, a metallic CF is formed due to the greater diffusivity of the metal cation than the oxygen anion. For OV-based RRAM, oxygen anions are much more diffusive than metal cations, and thus have central role on the device properties. On OV-based RRAM, the traps formed by the OVs are responsible for the CF in the *on*-state.

Electrochemical metallization RRAM

Diffusion and redox electrochemical reaction of metal cations are the base for the operation of ECM RRAMs. A metallic CF is formed during *set*, bringing the device from a high resistance state to a low resistance state. ECM RRAM can be further classified into three groups, depending on the origin of the metal cations used. In the first group, the metal cations are supplied only from the electrode. $Cu/SiO_2/Pt$ (45) and $Cu/Ta_2O_5/Pt$ (46) are examples of such systems, where Cu cations are from the Cu electrode. In the second group, the cations are supplied purely from the resistive layer. Systems like Pt/NiO/Pt (47) have the Ni cations coming from the NiO layer. Lastly, in system like $Ag/Ag_2Se/Pt$ (48), the metal cation Ag^+ can be supplied both from the electrode and the resistive layer.

Oxygen vacancies based RRAM

In contrast to ECM based RRAMs, where the metal cation has an important role in the CF formation, in OV-based RRAMs the metal cations are less diffusive or very difficult to precipitate and O^{2-} anions have the dominant effects on device performance. There are still lots of unknowns surrounding OV-based devices, as a result of the complicated physics involved. Nonetheless, several basic mechanisms and theories explain at least parts of the device behavior. In OV-based RRAMs, the CF formation process inside the device strongly depends on OVs. In these systems, OVs are typically more diffusive than metal cations. The *set* and *reset* usually involve OV generation and annihilation. The device has low

Figure 3 – Classification of RRAM devices

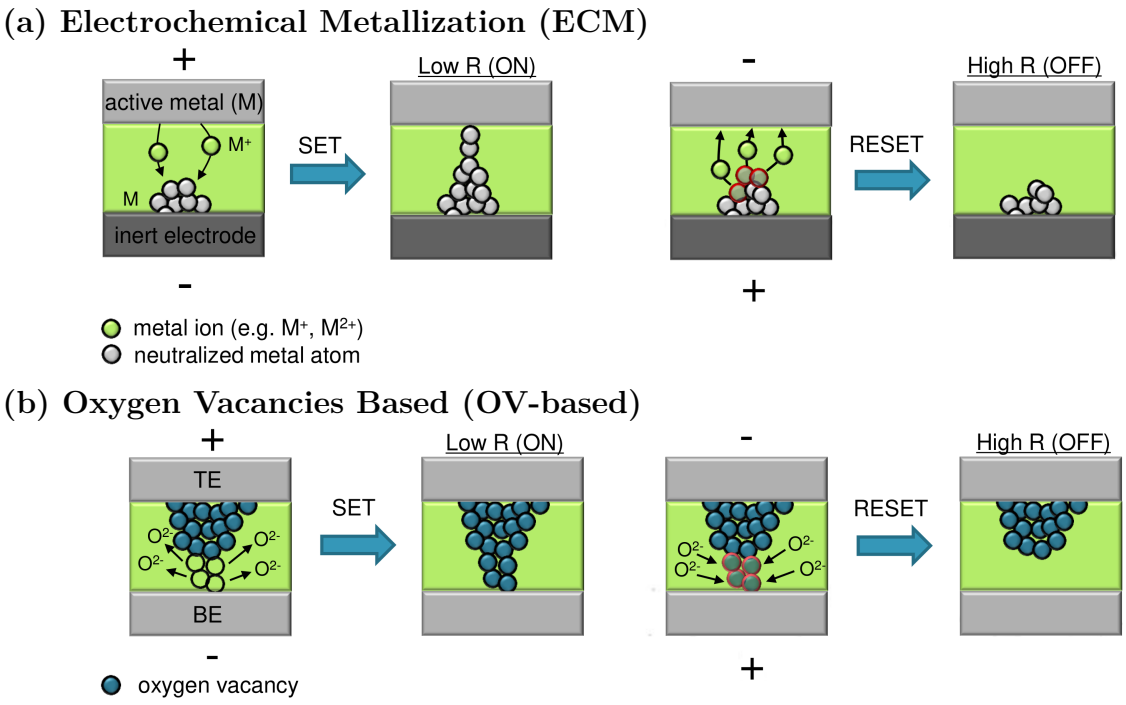

Source: Adapted from Jo(49) 2015.

resistance when the OV concentration is large. Conversely, the device resistance increases when the OV concentration is low. Therefore, how the OV affects the conductivity of the device and how the OV concentration can be controlled by applying voltage are keys in understanding the OV-based RRAMs physics.

OVs typically act as n-type dopants (50), mainly for low and moderate band gap materials like TiO_2 and Ta_2O_5. Thus, the electron concentration increases when the OV concentration increases. Conversely, OVs typically act as traps for large band gap materials, like HfO_2 and ZrO_2. In this case, electron hopping conduction becomes important.

1.1.2 TiO_2 use in RRAM technology

The first resistive switching in TiO_2 was observed by Chopra in 1965 (51). The films ($\approx$ 500 nm) were deposited by sputtering of Ti and then oxidized in an oxygen atmosphere. The resistive switching was considered purely electronic in nature, produced by an avalanche multiplication of carriers. Later in 1968, Argal (52) noted that the switching is not connected to a phase change, but did not clarify the mechanism behind the hystereretic behavior observed in TiO_2. The negative resistance oscillations associated with the resistive switching phenomena in TiO_2 were studied in the next decades. Taylor and Lalevic (53) developed a model to describe the *on*- and *off*-states in polycrystalline $Ti/TiO_2/Cr$ devices. They concluded that the small activation energy and the negative region of the I-V characteristic were linked to CFs formation in a charge limited current

condition. Parallel to these works on OV-based switching, Chudnovski et al. (54) reported resistive switching related to insulator-to-metal transitions (55) in electrochemically grown thin TiO_2 films.

Recently, the binary oxides — and in particular TiO_2 — came back in focus mainly due to the work of Bednorz's group (57), that demonstrated potential applications of resistive switching in RRAM technology. Choi et al. (37) related the resistive switching with CFs (see Fig. 4), observed in atomic layer-deposited TiO_2 films. Moreover, the nano CFs are composed by localized Ti_4O_7 crystals, according to Kwon et al. (20). Named after the notable chemist Arne Magnéli, X-oxides with stoichiometries that follow the rule X_nO_{2n-1} are called Magnéli phases. Thus, the *set* process is the formation of a conical pillar with a Magnéli phase induced by the electric field, which results in a short circuit between the two electrodes. Applying an electric field with opposite polarity gives rise to Joule heating at one end of the conical pillar causing it to become amorphous, and thus non-conducting. After *reset*, the amorphous region exhibits a random distribution of point defects that facilitates the next *set*/*reset* cycle.

Figure 4 – The Conductive Filament (CF) in TiO_2

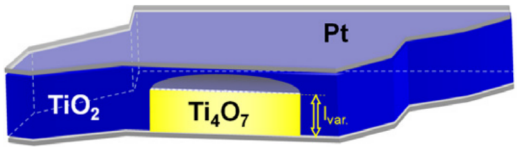

Source: Szot et al.(56) 2011.

The electrical field modulation of the oxygen vacancies migration along CFs is called *field programming*. The resultant oxygen deficiency on the thin TiO_2 layer close to the oxide/electrode interface changes the resistivity of the system. The electrode material also plays a role in the formation and breakup of CFs. As evidenced by Jeong et al. (34, 58), the interface Pt/TiO_2 has an influence on the CF size close to the thin TiO_2 insulating layer.

Podshivalova and Karpov (59) have studied the phase transformation from TiO to TiO_2 for SATP conditions (T = 25° C, P = 10^5 Pa), describing it as a step-process where the material transitions through a series of intermediary Magnéli phases. Contrary to the expected behavior, calculations show that the transformation from TiO to TiO_2 can be effective even at low temperatures; TiO_2 is created on the surface, with a rutile structure. Unfortunately no such calculation exists for our case of interest, namely the reverse solid-state reaction (reduction), which at moderate temperatures can lead to the transformation of TiO_2 into Ti_nO_{2n-1}.

There is consensus on the critical role of the diffusion of oxygen in the reduction of Magnéli phases and TiO_{2-x} (60, 61, 62, 63) and also on the formation and dissolution of the CFs (64, 65, 66). In fact, in almost every paper discussing resistance switching in

TiO_2 there are mentions on the role of OV migration induced by electric fields. Hence, when ion diffusion is relevant for the resistive switching its effectiveness depends on the mechanism behind ion migration. Particularly when operating at low temperatures, the migration is strongly influenced by Joule heating during *set*/*reset*.

1.1.3 Switching model

Even with a wide array of experimental data available, the underlying nature of resistive switching is, rather surprisingly, not well understood and a single physical description of resistive switching has not yet become available. However, researchers have demonstrated some fundamental properties which hold true for a wide range of RRAMs systems (39, 32, 33, 67, 68).

Considering a maximum current supplied to the device during the formation and rupture of the filaments, resistive switching can be controlled. This procedure allows for good predictability of the *on*- and *off*-states. A universal characteristic of the *on*-state was demonstrated, where all devices show a well defined resistance R_{on} in their *on*-state when the compliance current I_{set} follows the inverse rule:

$$R \sim \frac{1}{I_{set}}, \tag{1.1}$$

independent of the material composition, experimental configuration or *set* voltage applied (69). Conversely, the *reset* current I_{reset}, necessary to dissolve the CF, is inversely proportional to R, following the rule (39, 33, 69):

$$I_{reset} \sim \frac{1}{R} \sim I_{set}. \tag{1.2}$$

The inverse proportionality between I_{reset} and R can be understood as a law of constant voltage. At the *reset* voltage, the critical temperature threshold is achieved and the filament dissolution process is initiated; the result of oxidation and/or migration and diffusion (29, 69). The *reset* rule may be understood by the relation between the *reset* temperature and the ionic migration parameters, which are the diffusivity, mobility and activation energy (69).

In particular, bipolar RRAM devices evidence the role of ion migration induced by the electric field (44, 65, 70, 71, 72). The role of temperature on ion migration was also investigated in the context of the *set* and *reset* processes (73, 74). From the many physical models describing RRAM device operations, we will concentrate on one developed by Ielmini et al. (71, 74). The model is based on temperature- and field-accelerated ion migration, and *set* and *reset* processes are described by ionic/electronic conduction and Joule heating.

Figure 5 – Ion hopping

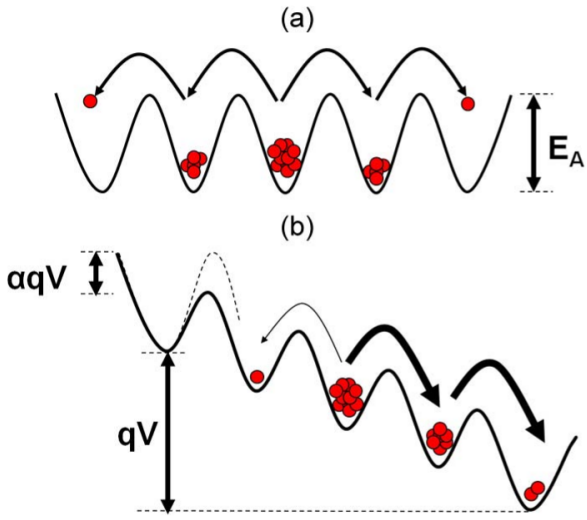

Source: Larentis et al.(75) 2012.

Note: Schematic of the potential energy landscape for ion hopping at (a) zero or (b) positive applied voltage.

Ion migration

The continuous CF connecting the opposite electrodes may be described as a highly doped region. Defects such as excess cations and OVs act as doping centers, affecting the local electrical and thermal conductivity values (74). Therefore, the defect migration induced by the local electrical field and the temperature rise caused by Joule heating are the physical processes necessary to describe the *set* and *reset* processes.

One can understand the ion migration as a random isotropic diffusion characterized by an uniform energy barrier E_a. This energy barrier is known as the *activation energy*, and is commonly used in stochastic formulations. It corresponds to the smallest amount of energy necessary to initiate some process — the ions hopping from defect to defect, in our case. The application of an electrical field $\mathbf{E}$ lowers the barrier in the direction of the field by a factor of αqV; where α is a constant that expresses the field strength, q is the elementary charge and V is the applied voltage. Conversely, due to the exponential relation between hopping probability and E_a an applied field greatly diminishes the migration against the field direction. Thus, a *drift* is induced in the direction of the field — as shown in Fig. 5.

Diffusion equations

The simplest equations derived to express diffusion were developed by Adolf Fick in the 19th century. Fick's first Law states that the molar flux J is proportional to the inverse of gradient of the concentration c:

$$J = -D\nabla c, \tag{1.3}$$

where D is the *diffusion coefficient*. From the mass continuity equation we can directly derive Fick's second law:

$$\frac{\partial c}{\partial t} = \nabla^2 Dc, \tag{1.4}$$

which states that the rate of change of concentration is proportional to the second spatial derivative at a certain point. A common approximation considers the diffusion coefficient independent of the concentration; it surely is, however, dependent of temperature. The ion diffusion is temperature activated, as depicted in Fig. 5, resulting in an exponential behavior:

$$D = D_0 e^{-\frac{E_A}{k_B T}}, \tag{1.5}$$

where D_0 is a constant, k_B is the Boltzmann constant and T is the temperature at a certain point in space.

Electric mobility

Now we focus on the electrical properties arising from the diffusion description of ion migration given above. The electric mobility is the capacity of charged particles, such as electrons or ion vacancies, to move through some material in response to the applied electric field. If an uniform electric field with magnitude E is applied, the drift velocity is given by:

$$v_d = \mu E, \tag{1.6}$$

where μ is the electric mobility. In 1905 working on the problem of Brownian motion, Einstein derived an unexpected connection between electrical mobility and diffusion:

$$\mu = \frac{qD}{k_B T}. \tag{1.7}$$

Corollary to this expression, both μ and D follow exponential relations with temperature. Therefore, ion migration is skewed toward high temperatures where both diffusion and ion mobility are enhanced.

1.2 Electron RBS technique

Electron Rutherford Backscattering Spectrometry (Electron RBS or ERBS) is a technique that uses high energy electrons to probe the near surface layer of the irradiated material. Similarly to RBS, this is achieved by analyzing the recoil energy transferred from the electron to a nucleus in a large-angle deflection. The main difficulty faced when using electrons as projectiles, is the extremely small recoil energies electrons transfer to target atoms. Resolving the transferred energy value is necessary to obtain information about the target structure and composition. Even in the optimal condition of backscattering geometry, the kinematic factor for collisions between an electron and a Si nucleus would be $k \approx 0.99992$. For 40 keV electrons, this correspond to a maximum energy loss of only 3.2 eV. Although small, this energy loss is large when compared to the energy resolution of a few 100's meV, commonly obtained in high-energy electron spectroscopy. In many respects backscattering of electrons is close to ion beam analysis, but in others the technique resembles spectroscopies such as XPS.

The experimental ERBS system is located at ANU, Canberra–Australia. First, the setup is succinctly described (Subsec. 1.2.1), then a theoretical background for spectrum analysis is presented (Subsec. 1.2.2).

1.2.1 Experimental Setup

The spectrometer is composed of an electron energy analyzer facing a high voltage semi-spherical chamber. A highly mono-energetic electron beam is also necessary, and is provided by either of the two available electron guns. Some details about the equipment are presented below.

Semi-spherical chamber

The sample holder located at the center is connected and surrounded by a semi-spherical chamber. The chamber is kept at high voltages, up to 39.5 keV. Because of the positive potential, electrons emerging from the electron gun are accelerated towards the sample holder. After scattering they may enter the analyzer, decelerating towards it.

Electron gun

The electrons are injected into the chamber through 2 electron guns in different geometries (see Fig. 6), with gun A the scattering angle is 120° and with gun B the scattering angle is 45°. In order to reduce the thermal spread, both are equipped with barium oxide cathodes; these electron emitters have low work function and hence operate at low temperatures. The electron guns are at a potential of −500 V, connected through a power supply with drift and ripple smaller than 50 meV. The beam impinges on the

Figure 6 – Electron Spectrometer

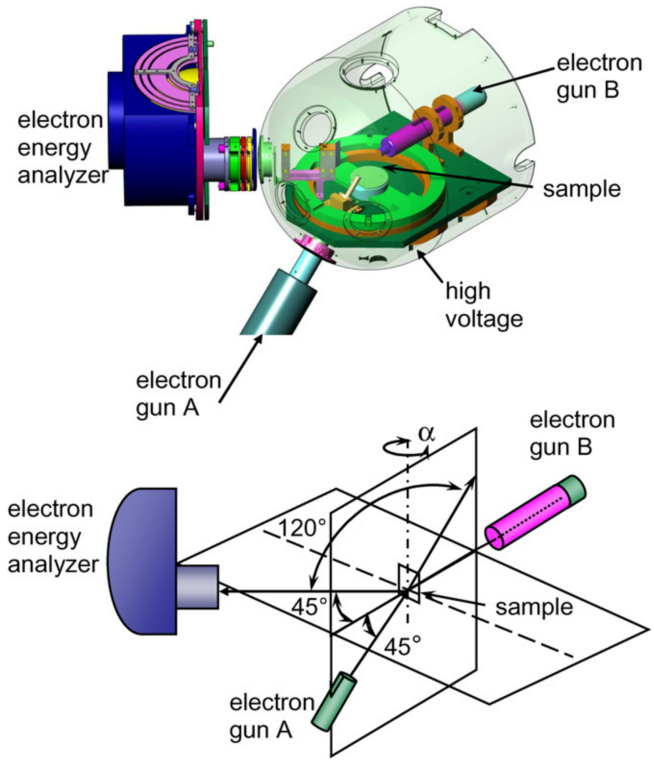

Source: Went e Vos(24) 2008.

sample with an intensity of few nA and is focused to form a spot with 0.2–0.4 mm in diameter.

Energy analyzer

After scattering in the sample, the electrons may enter a hemispherical analyzer located at a scattering angle θ. The analyzer is kept at -300 V in part using the same power supply of the guns. This configuration assures that voltages fluctuations in the power source affect the gun and the analyzer simultaneously, thus enhancing the energy resolution of the system. A set of slit lenses are used to decelerate the electrons from their high-energy, causing them to enter the analyzer with a kinetic energy of approximately 200 eV. The lenses are also used to form an image of the beam spot on the sample at the entrance plane of the hemispherical analyzer. At the exit of the analyzer, there is a position sensitive detector.

Detector

Electrons exiting the analyzer are detected by a micro-channel plate, which is necessary to amplify its signal, so its x-y coordinates can be determined. The position

Figure 7 – Camera image analysis

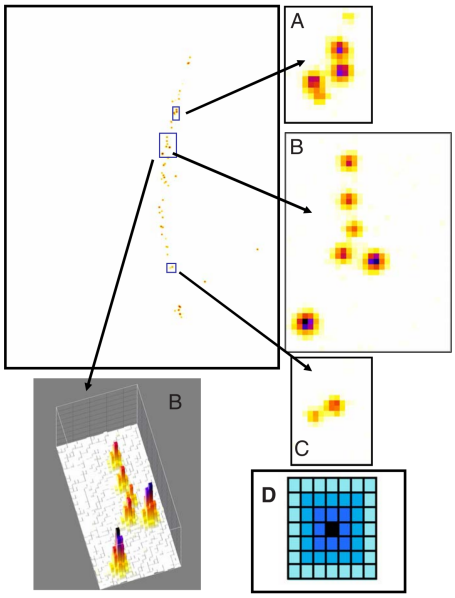

Source: Vos, Went e Weigold(25) 2009.

Note: On the top left pane, a colored 2D pixel map on the elastic peak energy region for the scattering of 1 keV electrons on Xe atoms. In A, B and C measurements of single electrons are shown in detail. In D we show the pixel area used in the integrator of counts during image processing.

of the resulting charge cloud is then read out by a phosphor screen coupled to a camera. Each shot has a very short time exposure, so there is no or rare overlap between the light emitted from separated events. Analysis of the resulting image can be used to identify individual electrons by reconstructing where the charge cloud hits the screen (see Fig. 7). The camera has an effective resolution of 640×430 pixels, and up to ≈ 230 frames/s are recorded. The x-coordinate relates to the energy of the electron, the y-coordinate to the phi angle. This configuration is capable of measuring electrons inside a 25 eV window simultaneously.

1.2.2 Physical description

The scattering of electrons on a crystal may be described in two different ways: as the diffraction of a wave interacting with many atoms that forms the crystal, or as a binary collision between the electron and some atom's nucleus. Using the first description, the electron momentum is absorbed by the whole crystal. As the nucleus has a mass much larger than the electron's, the change in momentum q of the electron is given by:

$$q = 2k_0 \sin\left(\frac{\theta}{2}\right), \tag{1.8}$$

Figure 8 – Scattering scheme

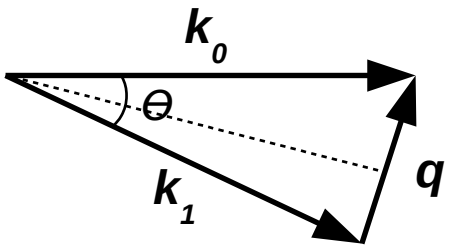

Source: Own authorship.

Note: After a scattering with angle θ, a part $\mathbf{q}$ of the electron initial momentum $\mathbf{k_0}$ is transferred to the target and the electron leaves with momentum $\mathbf{k_1}$.

for electrons with momentum $\mathbf{k_0}$ deflected over an angle θ. So in the case of diffraction, the recoil energy is $E_r = q^2/2m_c$ with m_c being the mass of the crystal. If the mass of the crystal is considered to be large ($m_c \to \infty$) the recoil energy approaches zero ($E_r \to 0$). In practical terms, this result means that no measurable change in energy would follow an electron scattering event. To verify such condition an experiment was already conducted in the 60's (76), using 30 keV electrons scattering in carbon through a 90° angle. This experiment was used to study a shift observed in the elastic-scattering peak, which appeared consistent with the energy transfer expected for interaction of electrons and free C atoms. Other more modern experiments were conducted too, with lower energy but better resolution, and similar results were reported (77, 78, 79). These observations show that large-angle scattering of electrons with an energy of a few keV's or more need to be treated as collisions between the electron and a single atom.

Momentum transfer in the collision

If the scattering is simply described as a collision between the high-energy electron and a target nucleus, the expression for the mean energy transferred from the projectile to the target is the recoiled energy $\overline{E_r} = \frac{q^2}{2m_a}$, where m_a is the mass of the target atom. From this relation it is possible to determine the mass of the target atom using high-energy electrons (> 1 keV) scattered over large angles ($> 90°$).

An analogous description is found in the study of neutron scattering, where similar momentum transfers are observed (80). Two approximations used in the aforementioned study will be applied here, the first is referred to as the incoherent approximation. It states that if $|q||r| >> 1$, where $|r|$ is the inter-atomic separation, the energy after the scattering is the one expected for scattering from a single atom in a molecule or crystal, rather than the molecule or crystal as a whole. The scattering interaction may be thought as scattering waves emanating from different atoms that have relative phases changing so

rapidly with r (due to thermal vibrations) that diffraction effects average out to zero. The second approximation is known as the plane-wave-impulse approximation, which states that typical collision times are so short that the target atom has no time to move, and thus its neighborhood may be neglected. Hence, the target atom is seen as a free atom by the high-energy projectile. If theses conditions apply, one can understand electron scattering as a Compton profile of the momentum distribution of the target atoms, and the transferred recoil energy from the electron to a free atom with momentum $\mathbf{p}$ is given by:

$$\overline{E_r} = \frac{(\mathbf{p}+\mathbf{q})^2}{2m_a} - \frac{p^2}{2m_a} = \frac{q^2}{2m_a} + \frac{\mathbf{p}\cdot\mathbf{q}}{m_a}. \tag{1.9}$$

Thus, the transferred recoil energy distribution correlates directly to the momentum distribution of the target atoms. For free atoms, i.e. noble gases, the momentum distribution is that of a classical gas. The distribution is such that $\int p_c^2/2m_a = 1/2kT$, for each of the momentum components $c = \{x, y, z\}$. Conversely, if the atom is bound to a molecule or solid, the momentum distribution is *not* that of a classical gas. In this case, the kinetic energy of the atoms and their momentum distribution are also affected by the rotational and vibrational properties of the molecule or solid. If the momentum distribution of all degrees of freedom have the same Gaussian-shape, then the elastic peak has a Doppler width σ_D given by (81, 82):

$$\sigma_D = \sqrt{\frac{4}{3}\langle E_{kin}\rangle\overline{E_r}} \tag{1.10}$$

where $\langle E_{kin}\rangle$ is the mean total kinetic energy of the atoms. If the mono-energetic electrons have a small enough spread, the width of the elastic peaks may be resolved. Thus, this experimental technique may be used to directly measure the mean kinetic energy of bound atoms, and by doing so one obtains the shape of the interatomic potential of the material.

Elastic differential cross section

The next step in the description is to account for the yield of all these electron scattering events, which is often described in terms of the Differential Cross Section (DCS). The elastic DCS is arguably the most important property of the model, as it expresses the probability of electrons being deflected by atoms over a specific angle.

Considering the already shown similarities between RBS and ERBS, a logical first cross section to consider is the Rutherford cross section. One can calculate the DCS using the First Born Approximation (FBA), describing the atom as a bare nucleus with atomic number Z. Expressed in atomic units, it equals to:

$$\frac{d\sigma}{d\Omega} = \frac{4\gamma^2 Z^2}{q^4}, \tag{1.11}$$

where the relativistic term, known as the Lorentz factor, is defined as $\gamma = (1 - v^2/c^2)^{-1/2}$. Here a simple Coulomb potential is considered, but in reality the potential felt by the

Figure 9 – Scattering Differential Cross Section

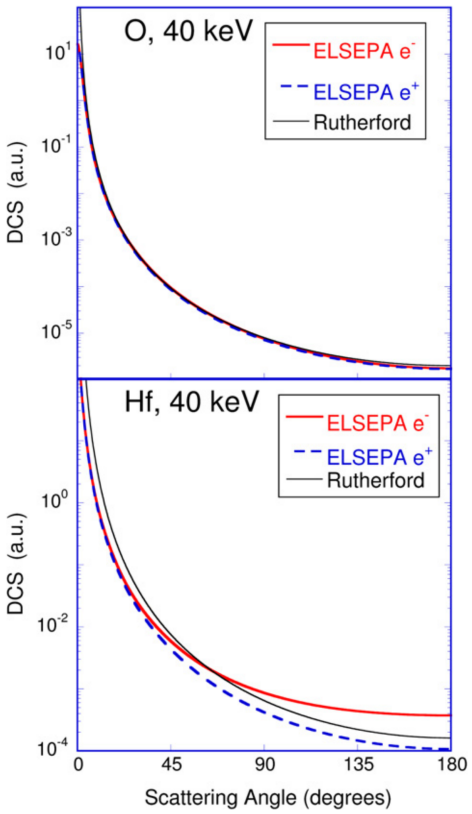

Source: Vos et al.(84) 2013.

scattered electron $V(r)$ is completely different (83). In the FBA, the DCS for a static potential can be written as:

$$\frac{d\sigma}{d\Omega} = \frac{1}{4\pi^2}\frac{k_1}{k_0}\left(\int e^{i\mathbf{q}\cdot\mathbf{r}}V(r)dr\right)^2. \tag{1.12}$$

Equation 1.12 still neglects exchange scattering, the effects of polarization of the atom and electronic absorption; which for keV electrons are reasonable approximations. For keV electrons scattering over large angles, the DCS deviates from Rutherford for light atoms by only 1%, but much more (factor of 2) for heavy atoms. Still, one must remember that the screening potential shape is very different from the potential Coulomb of the bare nucleus. The package ELSEPA (85), using the partial wave formalism, was used to account for the screening potential. This software gives a complete description of the scattering process, in which it uses many partial waves to calculate the DCS for both electrons and positrons with great precision (86).

The difference between DCS models decreases as the beam energy is increased, but it persist for heavier elements. Illustrating this effect the FBA, partial wave and Rutherford

calculated DCS are compared in the case of 40 keV electrons scattering from O and Hf (see Fig. 9). At this high-energy condition, DCSs for O show not much difference between models for all angles but near 0°. However, for the heavier Hf, large deviations are still present and differences of factors up to 5 are seen between positrons and electrons DCSs over large scattering angles. For the above reasons, ELSEPA scattering cross sections were used throughout this work.

2 Analysis of multi-layer samples

The main purpose of the physical description addressed in Subsection 1.2.2 is to understand the low energy loss region of ERBS spectra in order to improve ERBS analysis, in particular for O profiles in diffusional experiments. It was shown that considering some approximations the elastic peaks may be shaped after a Gaussian. From the peak mean energy loss one can obtain the target atom's mass, and from its width information about the target's kinetic energy. The last value used to parametrize a Gaussian peak is its area, which is related to the differential scattering cross section.

The electron beam may be seen as a flux of electrons impinging on the sample. As the electrons move through it, inelastic collisions with other electrons in the material decrease the initial flux intensity I_0 along the path. A parameter known as Inelastic Mean Free Path (IMFP) quantifies this *attenuation* effect as an exponential decay:

$$I(d) = I_0 \; e^{-\frac{d}{\lambda}}, \tag{2.1}$$

where I is the beam intensity after penetrating a length d and λ is the IMFP. The attenuation may be used to measure film thickness by comparing spectra taken in different geometries.

In one instance, the procedure was used in the analysis of a Si_3N_4 on top of TiO_2. The silicon nitrate film was deposited by Plasma-enhanced Chemical Vapor Deposition (PECVD), located at the Electronic Materials Engineering (EME) department in the ANU. The attenuation has a measurable effect on the elastic peaks' height if the film thickness is close to, or greater than the IMFP, which for 40 keV electrons travelling through oxides and nitrates is in the order of 10's of nms. In grazing geometries the effective thickness — i.e., the actual distance traveled by the moving electrons — is increased, and so is the attenuation of the elastic peak signals comming from the TiO_2 beneath. The simultaneous fitting of spectra obtained at different scattering angles leads to an estimate of the top film thickness. The fitting procedure was also employed in the analysis of carbon foil on top of Au substrate and TiO_2 film sputtered with 3 keV Xe^+ ions.

We have shown that multi-layer ERBS spectra can be fitted successfully in a very accurate way. The main question arises then if the extracted information is affected by any of the assumptions made, in particular the assumption of v-shaped trajectories, i.e. only a single large-angle scattering event. The effects of multiple scattering events were investigated further in the work described on Chapter 4. These results were published in the Journal of Electron Spectroscopy and Related Phenomena – Marmitt et al.(87) 2015.

3 Band gap measurements

Motivated by concerns about the condition of our films before/after annealing, we extended the multi-layer procedure to consider the band gap onset on the energy-loss spectrum. By monitoring the value of the band gap closely, one obtains valuable information about the quality of the TiO_2 during our diffusion experiments.

As discussed in Subsection 1.2.2, at the typical high energies used in ERBS experiments the electron-nucleon collisions are thought of as simple binary collisions. Energy transfers close to zero keep our analysis in the low energy loss region of the spectrum — below the band gap of most insulators. The band gap of some material is defined as the lowest energy necessary to promote an electron from the valence to the conductive band, which is the mechanism behind inelastic collisions described by the IMFP. On the ERBS spectrum, electrons measured with energy losses greater than the band gap may have suffered such inelastic collisions.

The fitting procedure described on Chapter 2 was extended to include band gap contributions, achieved through a background modeling. The background I_{bg} may be described by the following expression:

$$I_{bg} \sim (E - E_{gap})^A \tag{3.1}$$

where E_{gap} is the band gap and the exponent A is a constant that dictates the shape of the onset. In Reflection Electron Energy Loss Spectroscopy (REELS) experiments it is commonly assumed that for direct gap semiconductors $A \approx 0.5$ and for indirect gap semiconductors $A \approx 1.5$.

The richer description used enables the determination of the band gap for common oxides such as SiO_2, $CaCO_3$ and Li_2CO_3. The value for E_{gap} obtained for SiO_2 with $A = 1.5$ is 9 ± 0.2 eV, and is indeed consistent with the commonly accepted value of 8.9 eV. The good agreement for SiO_2 may indicate that this is the right exponent for analyzing REELS spectra for indirect gap semiconductors. For $CaCO_3$ compressed powder we obtained significant larger values (7.15 ± 0.2 eV for $A = 0.5$, 7.5 ± 0.2 eV for $A = 0.5$) than the literature value of 6 ± 0.35 eV. For Li_2CO_3 the obtained gap is between 7.1 ($A = 1.5$) and 7.6 eV ($A = 0.5$). It is important to note that the shape of the onset significantly change the obtained gap. These results were published in The Journal of Chemical Physics – Vos et al.(88) 2015.

4 Monte Carlo simulations

Next, we focused our efforts on the computational simulation of electron interactions with matter via a Monte Carlo algorithm. The implementations described below are extensions made to the PowerInteraction package, envisioning an unified simulation software for both ions and electrons. More information about the development of PowerInteraction is found on Appendix A.

First, the multiple elastic scattering effects in ERBS spectra were studied. The assumption of single scattering in ERBS is of doubtful validity, particularly for the case of high-Z atoms which have higher DCS values. The second step was to also add a stochastic description of the inelastic scattering process, which is essential to extract information from the high energy loss region of RHEELS spectra.

4.1 Elastic energy loss — ERBS

The procedure used for the simulation of elastic scattering is rather standard in Monte Carlo simulations. It considers only elastic scattering events, where the distance S to the next scattering event is determined by:

$$S = -\lambda_{elas} ln R, \tag{4.1}$$

where λ_{elas} is the elastic mean free path and R is uniformly distributed between 0 and 1. After each step, a next random number R decides from which atom the electron scatters.

For each elastic deflection, the recoil loss was calculated assuming that the atom was moving, as discussed on Subsection 1.2.2. The expression can be written as:

$$E_{recoil} = \frac{q^2}{2M} + \sigma_D. \tag{4.2}$$

After each iteration the electron moves S length in the direction given by its last scattering.

Our simulation was performed by a heavily modified version of the PowerInteraction software running a *connecting trajectories* algorithm. The procedure consists of first building many inward and outward trajectories, step by step as described above, and then pair them to form a scattering event. The weight of each connection is then evaluated based on the collision DCS diminished by the inelastic attenuation of the electron beam.

In order to validate our implementation, ERBS experiments and simulations were performed on Li_2CO_3, $CaCO_3$, TiO_2 and HfO_2. The two carbonate samples consisted of a powder pressed in a pill, the TiO_2 sample was obtained by thermal oxidation of Ti foil. The HfO_2 sample was a 60 nm thick HfO_2 layer grown by atomic layer deposition on a

silicon wafer. The spectra obtained in these experiments were compared to Monte Carlo simulations with the objective of investigating if the mean kinetic energies measured are significantly influenced by multiple scattering effects.

We have shown that multiple scattering hardly affects the obtained stoichiometry for compounds consisting of light and intermediate Z elements, but for compounds containing a large concentration of high Z elements, the effect is somewhat larger. However, simulations indicate that the peak width (and hence, extracted value of the mean kinetic energy of the atoms) is more sensitive to multiple scattering and the sensitivity increases when higher Z elements are part of the compound. These results were published in the Surface and Interface Analysis journal – Vos, Marmitt e Grande(89) 2016.

4.2 Inelastic energy loss — RHEELS

Up to this point, all ERBS analyses consider only energy losses of a few eV's; in effect, we have been neglecting the majority part of the energy spectrum. It has been known for a long time that electron energy loss measurements also contain information about the dielectric function of a material. In Transmission Electron Energy Loss Spectroscopy (TEELS) measurements of thin samples, where usually only a single inelastic event occurs, result in simple peaks in the energy loss spectrum. These peaks represent the characteristic energy losses which disperse with the transferred momentum q (selected by the detector angle), and are often called the Energy Loss Function (ELF) of the material. It can be written in the form $\mathrm{Im}[\frac{-1}{\epsilon(\omega,q)}]$, with ϵ as the dielectric function of the material under investigation and ω the energy loss.

In the case of RHEELS spectra analysis, which are a consequence of multiple

Figure 10 – Comparison of Monte Carlo and Analytical Mermin Convolutions

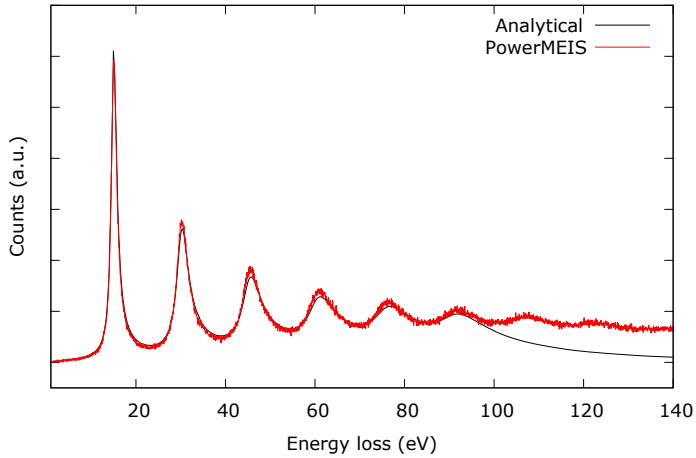

Source: Own authorship.

Figure 11 – PowerInteraction simulation for 5 and 40 keV electrons on bulk Al

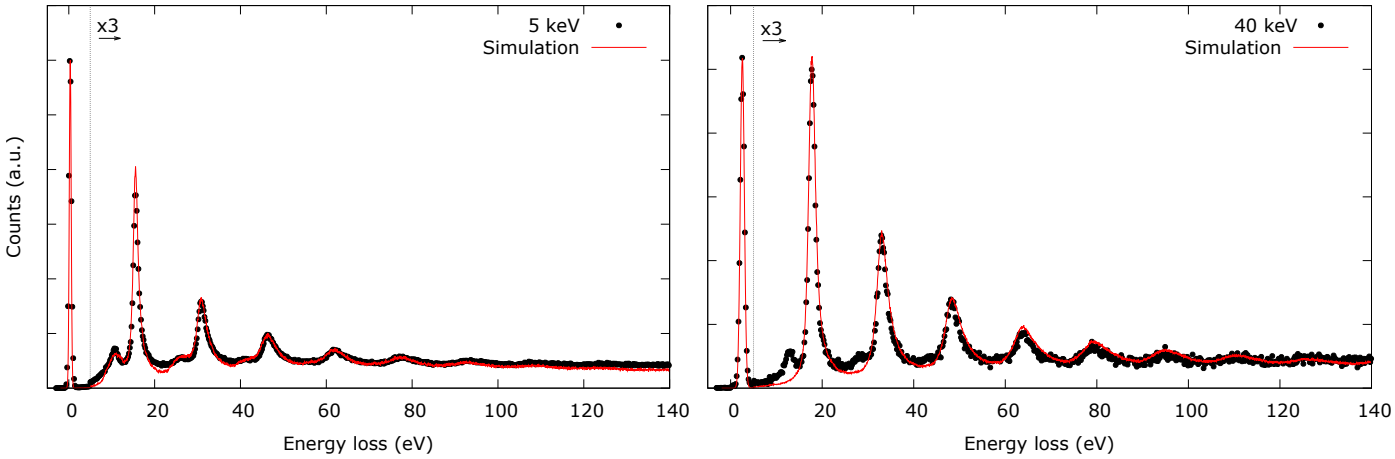

Source: Own authorship.

interactions of the projectile with the target, one has to make simplifying assumptions. One such simplification is assuming a simple functional form for the dielectric function. For example, for free-electron materials like aluminum, the dielectric function can be obtained from a Drude or Mermin plasmon excitation model.

The energy loss spectrum may exhibit bulk and surface plasmon excitations. The probability for bulk excitations is taken to be independent of the distance to the surface and is given by the differential inverse inelastic mean free path (DIIMFP) $W_b(\omega)$:

$$W_b(\omega) = \frac{1}{\pi E_0} \int_{q-}^{q+} \frac{dq}{q} \operatorname{Im}\left[\frac{-1}{\epsilon(\omega, q)}\right], \tag{4.3}$$

with $q_\pm = \sqrt{2E_0} \pm \sqrt{2(E_0 - \omega)}$ and E_0 the incoming energy. W_b is the probability of energy loss ω per unit path length.

The approach followed here seeks to complement the Monte Carlo procedure used in the case of elastic scattering. The probability of any inelastic energy loss is given by:

$$P = \int_0^\infty W_b(\omega) d\omega, \tag{4.4}$$

and the inelastic mean free path is simply $\lambda_{inel} = 1/P$. For material consisting of low Z materials, inelastic scattering is more probable $\lambda_{elas} \gg \lambda_{inel}$, and a number of inelastic events take place during each integration step S. Hence, the number of inelastic scattering is given by a Poisson distribution of mean S/λ_{inel}. For each inelastic event the energy loss ω is deducted from the projectile kinetic energy — value obtained by randomly selecting from the ELF distribution. A comparison of a 6-fold convolution of a single Mermin oscillator and our Monte Carlo approach for a thick film is showed in Fig. 10.

Considering the elastic and inelastic scattering events, one can simulate both the low energy loss peak analyzed in ERBS and the high energy loss structure observed by

RHEELS. One example of the capabilities of this implementation is presented in Fig. 11, where a bulk aluminum sample was measured with 5 and 40 keV electrons scattering at an angle of 135°. The ELF was described using 2 Mermin functions, as presented in Table 1.

Table 1 – Mermin oscillators

#	**A**	$\boldsymbol{\omega_0}$ (eV)	$\boldsymbol{\gamma}$ (eV)
Plasmon 1	0.97	15.1	0.95
Plasmon 2	0.03	157	1

The first plasmon can be clearly seen in the spectrum, since it has been (re)excited at energy intervals of 15.1 eV. The second plasmon is not seen on this measurement, but is necessary to obtain the correct height at the high energy loss region. The simulated spectra was normalized by the elastic peak intensity, and for both energies the simulated inelastic structure is in good agreement with the experimental data. These result are currently being prepared for publication.

5 Self-diffusion of O in TiO_2 films

As discussed in Subsection 1.1.1, OV-based RRAMs work via modification of CFs, composed of oxygen vacancies, due to a small change in stoichiometry during the formation and break-up processes. The characterization of the CFs requires the measurement of ~ 10 nm structures spread through areas with 100 μm or more. These constrains make the use of most ion beam techniques problematic, since the beam spot has a diameter more than 5 orders of magnitude larger than these structures. Here we take on a different approach, by directly studying the oxygen diffusion we seek to better understand the underlying physics involved in the formation and rupture of nano-scaled oxygen vacancies filaments.

Isotopic marking was used to obtain depth profiles induced by diffusion in samples initially composed by alternating layers of $Ti^{16}O_2$ and $Ti^{18}O_2$. Particular care was taken on the choice of experimental technique, since ion beam damage could contribute to the diffusion observed and adulterate the results. For this reason, the depth profiles were measured using the ERBS technique, described in detail in Chapter 1.2. For this experiment, two sets of TiO_2 bi-layer samples were deposited by sputtering on Si substrates, each consisting of layers with thicknesses of ≈ 20 nm and ≈ 55 nm. One layer of each sample was deposited with ^{18}O enriched water, in order to produce oxide films with 95% oxygen of its 18 mass isotope. These two sets of samples were covered with a ≈ 35 nm capping

Figure 12 – Preparation of TiO_2 samples

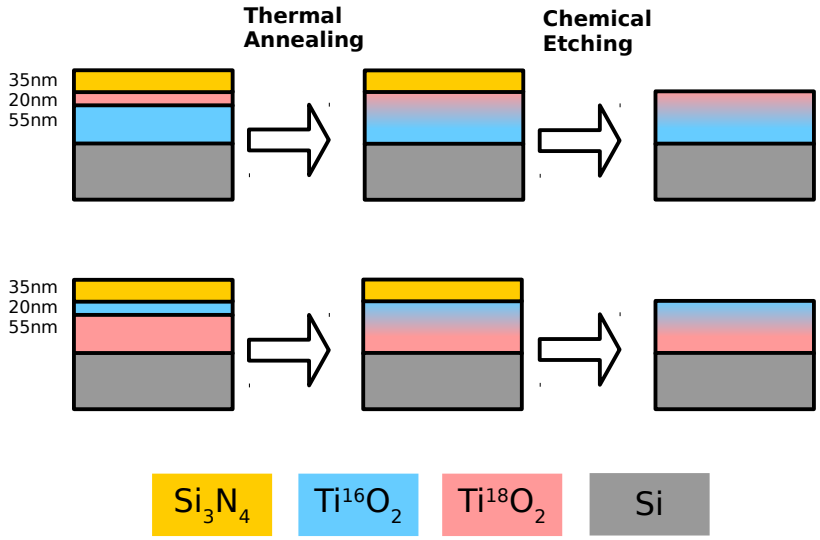

Source: Own authorship.

layer of Si_3N_4 in order to stop the oxygen exchange through the film surface, and then annealed in inert atmosphere of Ar for duration between 5–100 minutes and temperatures between 500–900 °C. The sample preparation procedure is sketched in Fig. 12.

After chemically removing the Si_3N_4 film, the samples were characterized by ERBS, RBS and NRP. In the ERBS spectra an energy shift is observed in the O elastic peak, that changes with the annealing temperature. This shift results from a change in concentration of ^{18}O and ^{16}O mixture occurring in the film near the surface. If we consider this a simple diffusion process, where Fick's laws of diffusion apply, then a diffusion profile can be calculated. Using the multi-layer analysis procedure developed on Chapter 2, we were able to obtain the diffusion lengths for each of the thermal treatments on our samples.

In order to cross check the results, RBS experiments were also conducted for one of the sets. Similarly with the ERBS spectra, oxygen peak shifts were also observed here. Next, simulations using PowerInteraction were performed, considering the same diffusion profiles obtained by ERBS. The simulations agreed beautifully with the RBS spectra.

The obtained diffusion values can be described quite well with a linear fit when plotted on a logarithmic scale. The slope of such Arrhenius plot is usually associated with the activation energy, and a value of about 1.05 eV is obtained in this case. By contrast, in experiments with longer thermal annealings ($t > 20$ hours) and higher temperatures ($T > 1000$ °C) the reported activation energies are close to 3 eV (60).

A useful picture to understand such discrepancy is by considering the effect of defects in the diffusion processes — particularly important in our case, since the sputtering deposition of TiO_2 used in our samples is known to produce films with a great number of defects. For short annealing times ($t < 1$ hour) fast defects, such as oxygen vacancies, are responsible for the lower activation energy. The vacancies defects and grain boundary are rapidly conformed, bringing the diffusion to a different regime. For long annealing times slow defects, such as Ti vacancies, are used by the oxygen atoms to drift through the TiO_2 matrix.

In summary, we measured the oxygen self diffusion in sputtered deposited thin TiO_2 films using the electron and ion Rutherford backscattering techniques. Particularly the ERBS technique has sensitivity and depth resolution to make possible the determination of the oxygen diffusion by ^{18}O labeling in samples that exhibit resistive switching and therefore can be used for RRAMs. This work was published in the Thin Solid Films journal – Marmitt et al.(90) 2017.

6 Conclusions

This thesis encompasses experiments that use electrons and ions. Their different interactions with matter are explored: the ERBS technique focuses on the elastic energy loss during a large angle scattering of electrons; RHEELS and RBS focus on the inelastic energy loss of the projectile during its path inside the material; and the NRP technique relies on a nuclear reaction boost to scattering cross sections. Thus, a combined analysis of complementary experimental techniques was used to shed some light on the diffusion processes that govern CF formation and rupturing in RRAMs. The understanding of electron interactions achieved during this work also expanded the simulation capabilities of our Monte Carlo software. All RBS, ERBS, RHEELS and NRP spectra presented here can be simulated and analyzed by the PowerInteraction code.

During the TiO_2 experiments concerning diffusion coefficients, the ERBS spectrum analysis was developed. The procedure was improved with multi-layer fitting, which considers the direct/indirect band gap onset, and Monte Carlo simulations.

The multi-layer fitting allows the ERBS technique to be used to determine thickness of many insulator films. The procedure was applied to the analysis of a carbon film deposited on Au, a layer of Si_3N_4 on top of TiO_2 and also on a TiO_2 film implanted with Xe atoms. In summary we have shown that the ERBS spectra of multi-layer samples can be represented by a sum of attenuated Gaussian peaks, each one corresponding to a different element. The spectra obtained at different experimental conditions can be well fitted with a single set of input parameters together with adjustments of background shape, energy resolution and exact zero position of the energy scale. This further establishes the capabilities of ERBS as a technique to analyze samples at depths much larger than the ones probed by XPS.

Additionally, by comparing ERBS spectra obtained at different beam energies – condition that exposes the onset of the inelastic structure of the spectrum – a band gap estimation can be evaluated. Band gap values for $CaCO_3$, Li_2CO_3 and SiO_2 were directly measured in this fashion, which also includes information about the direct/indirect nature of the gap. The choice of background is critical to the extraction of band gap values. Hence, any claim of precise band gap values obtained by such experiments without knowledge of the functional shape of the onset of the energy loss intensity should be treated with caution.

Simulations using a Monte Carlo algorithm were used to investigate multiple scattering effects in ERBS measurements of Li_2CO_3, $CaCO_3$, TiO_2 and HfO_2 samples. The stoichiometries obtained from the measurements are only marginally affected by multiple

scattering, but for the precise extraction of the mean kinetic energy of atoms, a Monte Carlo simulation is required. Hence, single scattering approximation becomes questionable for cases containing light and very heavy elements, such as HfO_2, where the effect of multiple scattering cannot be described as just a broadening but it causes a significant change in the shape of the structure.

The second simulation improvement was the addition of a Monte Carlo algorithm for inelastic scatterings. A careful analysis of the high electron energy loss region may provide information on the electronic structure of the sample, since the inelastic energy loss structure carries a fingerprint of the material dielectric function. By considering both the elastic and inelastic scattering events, one can simulate both the ERBS elastic peak and the RHEELS spectrum structure. As a proof of concept, a bulk aluminum sample was measured with 5 and 40 keV electrons. At both energies the simulated inelastic structure is in great accordance with the experimental data.

The picture provided by these analyses sets ERBS/RHEELS as a useful technique that gives atomic, structural and electrical properties simultaneously. The development of this technique allowed for accurate measurements of self-diffusion of oxygen in TiO_2, from which the diffusion activation energy and dynamics were derived.

Oxygen self-diffusion measurements were performed in samples composed by arranges of two TiO_2 layers, one of which was enriched with the 18 mass oxygen isotope. Induced by thermal treatments, the 16 and 18 isotopes of oxygen were mixed in between the two layers. Assuming a simple diffusion model, we were able to obtain diffusion profiles by comparing the oxygen isotopes relative peak intensities in the ERBS measured spectra. Then, from the logarithmic behavior of the diffusion coefficients one can obtain an activation energy of ≈ 1.05 eV for oxygen self-diffusion in our samples.

The activation energy obtained in this work is at odds with the majority of others reports, which point to values around 3 eV. Some important differences between the experiments are the longer duration ($t > 20$ h) and higher temperatures ($T > 1000°$ C) of the thermal annealing treatments reported in literature and the nature of the sample. One simplistic way to view these two behaviors is by considering the effects of defects in a crystal matrix. Soon after the thermal annealing starts, a huge amount of defects left over by the sputtering deposition are activated. Hence, oxygen vacancies may wade through the material much easier. Shortly after, vacancies defects and grain boundary become conformed and the diffusion enters in a different regime — these are the same defects that are responsible for the rapid formation of CFs in RRAMs.

Ion beam analysis provided complementary information: NRP measurements of the ^{18}O resonance gave information about the purity of the as-deposited films; and RBS technique was used to cross check the obtained diffusion coefficients. RBS simulations based on the diffusion profiles determined by ERBS were able to consistently fit the RBS

spectra, which confirms our results.

Bibliography

1 STRUKOV, D. B. et al. The missing memristor found. *Nature*, Nature Publishing Group, v. 453, n. 7191, p. 80–83, may 2008. Available at: <http://dx.doi.org/10.1038/nature06932>. Referenced 2 times on pages 19 and 20.

2 ROBINETT, W. et al. A memristor-based nonvolatile latch circuit. *Nanotechnology*, IOP Publishing, v. 21, n. 23, p. 235203, may 2010. Available at: <http://dx.doi.org/10.1088/0957-4484/21/23/235203>. Referenced on page 19.

3 VONTOBEL, P. O. et al. Writing to and reading from a nano-scale crossbar memory based on memristors. *Nanotechnology*, IOP Publishing, v. 20, n. 42, p. 425204, sep 2009. Available at: <http://dx.doi.org/10.1088/0957-4484/20/42/425204>. Referenced on page 19.

4 LAIHO, M.; LEHTONEN, E. Arithmetic operations within memristor-based analog memory. In: *2010 12th International Workshop on Cellular Nanoscale Networks and their Applications (CNNA 2010)*. Institute of Electrical & Electronics Engineers (IEEE), 2010. Available at: <http://dx.doi.org/10.1109/CNNA.2010.5430319>. Referenced on page 19.

5 MANEM, H. et al. Design considerations for variation tolerant multilevel CMOS/nano memristor memory. In: *Proceedings of the 20th symposium on Great lakes symposium on VLSI - GLSVLSI 10*. Association for Computing Machinery (ACM), 2010. Available at: <http://dx.doi.org/10.1145/1785481.1785548>. Referenced on page 19.

6 ESHRAGHIAN, K. et al. Memristor MOS content addressable memory (MCAM): Hybrid architecture for future high performance search engines. *IEEE Transactions on Very Large Scale Integration (VLSI) Systems*, Institute of Electrical & Electronics Engineers (IEEE), v. 19, n. 8, p. 1407–1417, aug 2011. Available at: <http://dx.doi.org/10.1109/TVLSI.2010.2049867>. Referenced on page 19.

7 KIM, H. et al. Memristor-based multilevel memory. In: *2010 12th International Workshop on Cellular Nanoscale Networks and their Applications (CNNA 2010)*. Institute of Electrical & Electronics Engineers (IEEE), 2010. Available at: <http://dx.doi.org/10.1109/CNNA.2010.5430320>. Referenced on page 19.

8 XIA, Q. et al. Memristor-CMOS hybrid integrated circuits for reconfigurable logic. *Nano Letters*, American Chemical Society (ACS), v. 9, n. 10, p. 3640–3645, oct 2009. Available at: <http://dx.doi.org/10.1021/nl901874j>. Referenced on page 19.

9 JO, S. H. et al. Nanoscale memristor device as synapse in neuromorphic systems. *Nano Letters*, American Chemical Society (ACS), v. 10, n. 4, p. 1297–1301, apr 2010. Available at: <http://dx.doi.org/10.1021/nl904092h>. Referenced on page 19.

10 AFIFI, A. et al. Efficient hybrid CMOS-nano circuit design for spiking neurons and memristive synapses with STDP. *IEICE Transactions on Fundamentals of Electronics, Communications and Computer Sciences*, Institute of Electronics, Information and Communications Engineers (IEICE), E93-A, n. 9, p. 1670–1677, 2010. Available at: <http://dx.doi.org/10.1587/transfun.E93.A.1670>. Referenced on page 19.

11 MUTHUSWAMY, B. *Memristor Based Chaotic Circuits*. [S.l.], 2009. Available at: <http://www.eecs.berkeley.edu/Pubs/TechRpts/2009/EECS-2009-6.html>. Referenced on page 19.

12 QI-SHUI, Z.; YONG-BIN, Y.; JUE-BANG, Y. Fuzzy modeling and impulsive control of a memristor-based chaotic system. *Chinese Physics Letters*, IOP Publishing, v. 27, n. 2, p. 020501, feb 2010. Available at: <http://dx.doi.org/10.1088/0256-307X/27/2/020501>. Referenced on page 19.

13 JO, S. H.; KIM, K.-H.; LU, W. Programmable resistance switching in nanoscale two-terminal devices. *Nano Letters*, American Chemical Society (ACS), v. 9, n. 1, p. 496–500, jan 2009. Available at: <http://dx.doi.org/10.1021/nl803669s>. Referenced on page 19.

14 SHIN, S.; KIM, K.; KANG, S.-M. Memristor-based fine resolution programmable resistance and its applications. In: *2009 International Conference on Communications, Circuits and Systems*. Institute of Electrical & Electronics Engineers (IEEE), 2009. Available at: <http://dx.doi.org/10.1109/ICCCAS.2009.5250376>. Referenced on page 19.

15 RAJA, T.; MOURAD, S. Digital logic implementation in memristor-based crossbars. In: *2009 International Conference on Communications, Circuits and Systems*. Institute of Electrical & Electronics Engineers (IEEE), 2009. Available at: <http://dx.doi.org/10.1109/ICCCAS.2009.5250374>. Referenced on page 19.

16 HU, X. et al. Memristive crossbar array with applications in image processing. *Science China Information Sciences*, Springer Science + Business Media, v. 55, n. 2, p. 461–472, dec 2011. Available at: <http://dx.doi.org/10.1007/s11432-011-4410-9>. Referenced on page 19.

17 DONGALE, T. D. et al. *TiO_2 based Nanostructured Memristor for RRAM and Neuromorphic Applications: A Simulation Approach*. 2016. ArXiv:1601.06503v1. Referenced on page 19.

18 MIAO, F. et al. Continuous electrical tuning of the chemical composition of TaO_x -based memristors. *ACS Nano*, American Chemical Society (ACS), v. 6, n. 3, p. 2312–2318, mar 2012. Available at: <http://dx.doi.org/10.1021/nn2044577>. Referenced on page 20.

19 MIAO, F. et al. Anatomy of a nanoscale conduction channel reveals the mechanism of a high-performance memristor. *Adv. Mater.*, Wiley-Blackwell, v. 23, n. 47, p. 5633–5640, nov 2011. Available at: <http://dx.doi.org/10.1002/adma.201103379>. Referenced on page 20.

20 KWON, D.-H. et al. Atomic structure of conducting nanofilaments in TiO_2 resistive switching memory. *Nature Nanotech*, Nature Publishing Group, v. 5, n. 2, p. 148–153, jan 2010. Available at: <http://dx.doi.org/10.1038/nnano.2009.456>. Referenced 3 times on pages 20, 23, and 26.

21 BRACHT, H. et al. Self- and foreign-atom diffusion in semiconductor isotope heterostructures. II. experimental results for silicon. *Phys. Rev. B*, American Physical Society (APS), v. 75, n. 3, jan 2007. Available at: <http://dx.doi.org/10.1103/PhysRevB.75.035211>. Referenced on page 20.

22 VOS, M. et al. Oxygen self-diffusion in HfO_2 studied by electron spectroscopy. *Phys. Rev. Lett.*, American Physical Society (APS), v. 112, n. 17, apr 2014. Available at: <http://dx.doi.org/10.1103/PhysRevLett.112.175901>. Referenced on page 21.

23 WENT, M. R.; VOS, M. Investigation of binary compounds using electron rutherford backscattering. *Appl. Phys. Lett.*, AIP Publishing, v. 90, n. 7, p. 072104, 2007. Available at: <http://dx.doi.org/10.1063/1.2535986>. Referenced on page 21.

24 WENT, M.; VOS, M. Rutherford backscattering using electrons as projectiles: Underlying principles and possible applications. *Nuclear Instruments and Methods in Physics Research Section B: Beam Interactions with Materials and Atoms*, Elsevier BV, v. 266, n. 6, p. 998–1011, mar 2008. Available at: <http://dx.doi.org/10.1016/j.nimb.2008.01.059>. Referenced 2 times on pages 21 and 31.

25 VOS, M.; WENT, M. R.; WEIGOLD, E. Electron spectroscopy using two-dimensional electron detection and a camera in a single electron counting mode. *Rev. Sci. Instrum.*, AIP Publishing, v. 80, n. 6, p. 063302, 2009. Available at: <http://dx.doi.org/10.1063/1.3152366>. Referenced 2 times on pages 21 and 32.

26 HASAN, M. et al. Uniform resistive switching with a thin reactive metal interface layer in metal-$la_{0.7}ca_{0.3}MnO_3$-metal heterostructures. *Appl. Phys. Lett.*, AIP Publishing, v. 92, n. 20, p. 202102, 2008. Available at: <http://dx.doi.org/10.1063/1.2932148>. Referenced on page 23.

27 SAWA, A. Resistive switching in transition metal oxides. *Materials Today*, Elsevier BV, v. 11, n. 6, p. 28–36, jun 2008. Available at: <http://dx.doi.org/10.1016/S1369-7021(08)70119-6>. Referenced on page 23.

28 WASER, R.; AONO, M. Nanoionics-based resistive switching memories. *Nature Materials*, Nature Publishing Group, v. 6, n. 11, p. 833–840, nov 2007. Available at: <http://dx.doi.org/10.1038/nmat2023>. Referenced on page 23.

29 RUSSO, U. et al. Filament conduction and reset mechanism in NiO-based resistive-switching memory (RRAM) devices. *IEEE Trans. Electron Devices*, Institute of Electrical & Electronics Engineers (IEEE), v. 56, n. 2, p. 186–192, feb 2009. Available at: <http://dx.doi.org/10.1109/TED.2008.2010583>. Referenced 2 times on pages 23 and 27.

30 STRACHAN, J. P. et al. Direct identification of the conducting channels in a functioning memristive device. *Adv. Mater.*, Wiley-Blackwell, v. 22, n. 32, p. 3573–3577, jun 2010. Available at: <http://dx.doi.org/10.1002/adma.201000186>. Referenced on page 23.

31 PARK, G.-S. et al. Observation of electric-field induced ni filament channels in polycrystalline NiO_x film. *Appl. Phys. Lett.*, AIP Publishing, v. 91, n. 22, p. 222103, 2007. Available at: <http://dx.doi.org/10.1063/1.2813617>. Referenced on page 23.

32 KINOSHITA, K. et al. Reduction in the reset current in a resistive random access memory consisting of NiO_x brought about by reducing a parasitic capacitance. *Appl. Phys. Lett.*, AIP Publishing, v. 93, n. 3, p. 033506, 2008. Available at: <http://dx.doi.org/10.1063/1.2959065>. Referenced 2 times on pages 23 and 27.

33 NARDI, F. et al. Control of filament size and reduction of reset current below 10μa in NiO resistance switching memories. *Solid-State Electronics*, Elsevier BV, v. 58, n. 1, p. 42–47, apr 2011. Available at: <http://dx.doi.org/10.1016/j.sse.2010.11.031>. Referenced 2 times on pages 23 and 27.

34 JEONG, D. S.; SCHROEDER, H.; WASER, R. Coexistence of bipolar and unipolar resistive switching behaviors in a pt/TiO_2/pt stack. *Electrochemical and Solid-State Letters*, The Electrochemical Society, v. 10, n. 8, p. G51, 2007. Available at: <http://dx.doi.org/10.1149/1.2742989>. Referenced 2 times on pages 23 and 26.

35 GOUX, L. et al. Coexistence of the bipolar and unipolar resistive-switching modes in NiO cells made by thermal oxidation of ni layers. *J. Appl. Phys.*, AIP Publishing, v. 107, n. 2, p. 024512, 2010. Available at: <http://dx.doi.org/10.1063/1.3275426>. Referenced on page 23.

36 LEE, S. et al. Coexistence of unipolar and bipolar resistive switching characteristics in ZnO thin films. *J. Appl. Phys.*, AIP Publishing, v. 108, n. 7, p. 076101, 2010. Available at: <http://dx.doi.org/10.1063/1.3489882>. Referenced on page 23.

37 CHOI, B. J. et al. Resistive switching mechanism of TiO_2 thin films grown by atomic-layer deposition. *J. Appl. Phys.*, AIP Publishing, v. 98, n. 3, p. 033715, 2005. Available at: <http://dx.doi.org/10.1063/1.2001146>. Referenced 2 times on pages 23 and 26.

38 KIM, S.; CHOI, Y.-K. A comprehensive study of the resistive switching mechanism in Al / TiO_x / TiO_2 / Al-structured RRAM. *IEEE Trans. Electron Devices*, Institute of Electrical & Electronics Engineers (IEEE), v. 56, n. 12, p. 3049–3054, dec 2009. Available at: <http://dx.doi.org/10.1109/TED.2009.2032597>. Referenced on page 23.

39 LEE, J. et al. Diode-less nano-scale ZrO_x / HfO_x RRAM device with excellent switching uniformity and reliability for high-density cross-point memory applications. In: *2010 International Electron Devices Meeting*. Institute of Electrical & Electronics Engineers (IEEE), 2010. Available at: <http://dx.doi.org/10.1109/IEDM.2010.5703393>. Referenced 2 times on pages 23 and 27.

40 AHN, S.-E. et al. Write current reduction in transition metal oxide based resistance change memory. *Adv. Mater.*, Wiley-Blackwell, v. 20, n. 5, p. 924–928, mar 2008. Available at: <http://dx.doi.org/10.1002/adma.200702081>. Referenced on page 23.

41 IELMINI, D.; NARDI, F.; CAGLI, C. Resistance-dependent amplitude of random telegraph-signal noise in resistive switching memories. *Appl. Phys. Lett.*, AIP Publishing, v. 96, n. 5, p. 053503, 2010. Available at: <http://dx.doi.org/10.1063/1.3304167>. Referenced on page 23.

42 PARK, J. et al. Investigation of state stability of low-resistance state in resistive memory. *IEEE Electron Device Lett.*, Institute of Electrical & Electronics Engineers (IEEE), v. 31, n. 5, p. 485–487, may 2010. Available at: <http://dx.doi.org/10.1109/LED.2010.2042677>. Referenced on page 23.

43 IELMINI, D. et al. Size-dependent retention time in NiO-based resistive-switching memories. *IEEE Electron Device Lett.*, Institute of Electrical & Electronics Engineers (IEEE), v. 31, n. 4, p. 353–355, apr 2010. Available at: <http://dx.doi.org/10.1109/LED.2010.2040799>. Referenced on page 23.

44 WASER, R. et al. Redox-based resistive switching memories - nanoionic mechanisms, prospects, and challenges. *Adv. Mater.*, Wiley-Blackwell, v. 21, n. 25-26, p. 2632–2663, jul 2009. Available at: <http://dx.doi.org/10.1002/adma.200900375>. Referenced 2 times on pages 24 and 27.

45 SCHINDLER, C.; STAIKOV, G.; WASER, R. Electrode kinetics of Cu-SiO_2-based resistive switching cells: Overcoming the voltage-time dilemma of electrochemical metallization memories. *Appl. Phys. Lett.*, AIP Publishing, v. 94, n. 7, p. 072109, 2009. Available at: <http://dx.doi.org/10.1063/1.3077310>. Referenced on page 24.

46 SAKAMOTO, T. et al. A ta_2o_5 solid-electrolyte switch with improved reliability. In: *2007 IEEE Symposium on VLSI Technology*. Institute of Electrical & Electronics Engineers (IEEE), 2007. Available at: <http://dx.doi.org/10.1109/VLSIT.2007.4339718>. Referenced on page 24.

47 YUN, J.-B. et al. Random and localized resistive switching observation in Pt/NiO/Pt. *physica status solidi (RRL) – Rapid Research Letters*, Wiley-Blackwell, v. 1, n. 6, p. 280–282, nov 2007. Available at: <http://dx.doi.org/10.1002/pssr.200701205>. Referenced on page 24.

48 JANG, J. et al. Resistance switching characteristics of solid electrolyte chalcogenide Ag_2Se nanoparticles for flexible nonvolatile memory applications. *Adv. Mater.*, Wiley-Blackwell, v. 24, n. 26, p. 3573–3576, jun 2012. Available at: <http://dx.doi.org/10.1002/adma.201200671>. Referenced on page 24.

49 JO, S. H. Recent progress in RRAM materials and devices. In: *SEMICON Korea 2015*. [S.l.: s.n.], 2015. Referenced on page 25.

50 KNAUTH, P.; TULLER, H. L. Electrical and defect thermodynamic properties of nanocrystalline titanium dioxide. *J. Appl. Phys.*, AIP Publishing, v. 85, n. 2, p. 897, 1999. Available at: <http://dx.doi.org/10.1063/1.369208>. Referenced on page 25.

51 CHOPRA, K. L. Avalanche-induced negative resistance in thin oxide films. *Journal of Applied Physics*, AIP Publishing, v. 36, n. 1, p. 184–187, jan 1965. Available at: <http://dx.doi.org/10.1063/1.1713870>. Referenced on page 25.

52 ARGALL, F. Switching phenomena in titanium oxide thin films. *Solid-State Electronics*, Elsevier BV, v. 11, n. 5, p. 535–541, may 1968. Available at: <http://dx.doi.org/10.1016/0038-1101(68)90092-0>. Referenced on page 25.

53 TAYLOR, G.; LALEVIC, B. RF relaxation oscillations in polycrystalline TiO_2 thin films. *Solid-State Electronics*, Elsevier BV, v. 19, n. 8, p. 669–674, aug 1976. Available at: <http://dx.doi.org/10.1016/0038-1101(76)90143-X>. Referenced on page 25.

54 CHUDNOVSKII, F. et al. Electroforming and switching in oxides of transition metals: The role of metal–insulator transition in the switching mechanism. *Journal of Solid State Chemistry*, Elsevier BV, v. 122, n. 1, p. 95–99, feb 1996. Available at: <http://dx.doi.org/10.1006/jssc.1996.0087>. Referenced on page 26.

55 IMADA, M.; FUJIMORI, A.; TOKURA, Y. Metal-insulator transitions. *Reviews of Modern Physics*, American Physical Society (APS), v. 70, n. 4, p. 1039–1263, oct 1998. Available at: <http://dx.doi.org/10.1103/RevModPhys.70.1039>. Referenced on page 26.

56 SZOT, K. et al. TiO_2 — a prototypical memristive material. *Nanotechnology*, IOP Publishing, v. 22, n. 25, p. 254001, may 2011. Available at: <http://dx.doi.org/10.1088/0957-4484/22/25/254001>. Referenced on page 26.

57 BECK, A. et al. Reproducible switching effect in thin oxide films for memory applications. *Appl. Phys. Lett.*, AIP Publishing, v. 77, n. 1, p. 139, 2000. Available at: <http://dx.doi.org/10.1063/1.126902>. Referenced on page 26.

58 JEONG, D. S.; SCHROEDER, H.; WASER, R. Mechanism for bipolar switching in a pt / TiO_2 / pt resistive switching cell. *Phys. Rev. B*, American Physical Society (APS), v. 79, n. 19, may 2009. Available at: <http://dx.doi.org/10.1103/PhysRevB.79.195317>. Referenced on page 26.

59 PODSHIVALOVA, A. K.; KARPOV, I. K. Thermodynamic analysis of the stability of titanium oxides in the TiO-TiO_2 range. *Russian Journal of Inorganic Chemistry*, Pleiades Publishing Ltd, v. 52, n. 7, p. 1147–1150, jul 2007. Available at: <http://dx.doi.org/10.1134/S0036023607070273>. Referenced on page 26.

60 ARITA, M. et al. Depth profile measurement by secondary ion mass spectrometry for determining the tracer diffusivity of oxygen in rutile. *Journal of the American Ceramic Society*, Wiley-Blackwell, v. 62, n. 9-10, p. 443–446, sep 1979. Available at: <http://dx.doi.org/10.1111/j.1151-2916.1979.tb19101.x>. Referenced 2 times on pages 26 and 46.

61 BAGSHAW, A.; HYDE, B. Oxygen tracer diffusion in the magnéli phases Ti_nO_{2n-1}. *Journal of Physics and Chemistry of Solids*, Elsevier BV, v. 37, n. 9, p. 835–838, jan 1976. Available at: <http://dx.doi.org/10.1016/0022-3697(76)90058-5>. Referenced on page 26.

62 MILLOT, F. Oxygen self-diffusion in non-stoichiometric rutile TiO_{2-x} at high temperature. *Solid State Ionics*, Elsevier BV, v. 28-30, p. 1344–1348, sep 1988. Available at: <http://dx.doi.org/10.1016/0167-2738(88)90384-0>. Referenced on page 26.

63 HOSHINO, K.; PETERSON, N.; WILEY, C. Diffusion and point defects in TiO_{2-x}. *Journal of Physics and Chemistry of Solids*, Elsevier BV, v. 46, n. 12, p. 1397–1411, jan 1985. Available at: <http://dx.doi.org/10.1016/0022-3697(85)90079-4>. Referenced on page 26.

64 MEYER, R.; LIEDTKE, R.; WASER, R. Oxygen vacancy migration and time-dependent leakage current behavior of $ba_{0.3}sr_{0.7}TiO_3$ thin films. *Appl. Phys. Lett.*, AIP Publishing, v. 86, n. 11, p. 112904, 2005. Available at: <http://dx.doi.org/10.1063/1.1874313>. Referenced on page 26.

65 JANOUSCH, M. et al. Role of oxygen vacancies in cr-doped $SrTiO_3$ for resistance-change memory. *Adv. Mater.*, Wiley-Blackwell, v. 19, n. 17, p. 2232–2235, sep 2007. Available at: <http://dx.doi.org/10.1002/adma.200602915>. Referenced 2 times on pages 26 and 27.

66 AONO, M.; HASEGAWA, T. The atomic switch. *Proceedings of the IEEE*, Institute of Electrical & Electronics Engineers (IEEE), v. 98, n. 12, p. 2228–2236, dec 2010. Available at: <http://dx.doi.org/10.1109/JPROC.2010.2061830>. Referenced on page 26.

67 LEE, H. Y. et al. Low power and high speed bipolar switching with a thin reactive ti buffer layer in robust HfO2 based RRAM. In: *2008 IEEE International Electron Devices Meeting*. Institute of Electrical & Electronics Engineers (IEEE), 2008. Available at: <http://dx.doi.org/10.1109/IEDM.2008.4796677>. Referenced on page 27.

68 KAMALANATHAN, D. et al. Voltage-driven on-off transition and tradeoff with program and erase current in programmable metallization cell (PMC) memory. *IEEE Electron Device Lett.*, Institute of Electrical & Electronics Engineers (IEEE), v. 30, n. 5, p. 553–555, may 2009. Available at: <http://dx.doi.org/10.1109/LED.2009.2016991>. Referenced on page 27.

69 IELMINI, D.; NARDI, F.; CAGLI, C. Universal reset characteristics of unipolar and bipolar metal-oxide RRAM. *IEEE Trans. Electron Devices*, Institute of Electrical & Electronics Engineers (IEEE), v. 58, n. 10, p. 3246–3253, oct 2011. Available at: <http://dx.doi.org/10.1109/TED.2011.2161088>. Referenced on page 27.

70 MEYER, R. et al. Oxide dual-layer memory element for scalable non-volatile cross-point memory technology. In: *2008 9th Annual Non-Volatile Memory Technology Symposium (NVMTS)*. Institute of Electrical & Electronics Engineers (IEEE), 2008. Available at: <http://dx.doi.org/10.1109/NVMT.2008.4731194>. Referenced on page 27.

71 IELMINI, D. Modeling the universal set/reset characteristics of bipolar RRAM by field- and temperature-driven filament growth. *IEEE Trans. Electron Devices*, Institute of Electrical & Electronics Engineers (IEEE), v. 58, n. 12, p. 4309–4317, dec 2011. Available at: <http://dx.doi.org/10.1109/TED.2011.2167513>. Referenced on page 27.

72 YU, S.; GUAN, X.; WONG, H.-S. P. On the stochastic nature of resistive switching in metal oxide RRAM: Physical modeling, monte carlo simulation, and experimental characterization. In: *2011 International Electron Devices Meeting*. Institute of Electrical & Electronics Engineers (IEEE), 2011. Available at: <http://dx.doi.org/10.1109/IEDM.2011.6131572>. Referenced on page 27.

73 MENZEL, S. et al. Origin of the ultra-nonlinear switching kinetics in oxide-based resistive switches. *Adv. Funct. Mater.*, Wiley-Blackwell, v. 21, n. 23, p. 4487–4492, sep 2011. Available at: <http://dx.doi.org/10.1002/adfm.201101117>. Referenced on page 27.

74 IELMINI, D. Filamentary-switching model in RRAM for time, energy and scaling projections. In: *2011 International Electron Devices Meeting*. Institute of Electrical & Electronics Engineers (IEEE), 2011. Available at: <http://dx.doi.org/10.1109/IEDM.2011.6131571>. Referenced 2 times on pages 27 and 28.

75 LARENTIS, S. et al. Resistive switching by voltage-driven ion migration in bipolar RRAM part II: Modeling. *IEEE Trans. Electron Devices*, Institute of Electrical & Electronics Engineers (IEEE), v. 59, n. 9, p. 2468–2475, sep 2012. Available at: <http://dx.doi.org/10.1109/TED.2012.2202320>. Referenced on page 28.

76 BOERSCH, H.; WOLTER, R.; SCHOENEBECK, H. Elastische energieverluste kristallgestreuter elektronen. *Zeitschrift fur Physik*, Springer Science Business Media, v. 199, n. 1, p. 124–134, feb 1967. Available at: <http://dx.doi.org/10.1007/BF01326021>. Referenced on page 33.

77 GERGELY, G. et al. Recoil broadening of the elastic peak in electron spectroscopy. *Vacuum*, Elsevier BV, v. 61, n. 2-4, p. 107–111, may 2001. Available at: <http://dx.doi.org/10.1016/S0042-207X(00)00464-4>. Referenced on page 33.

78 VARGA, D. et al. Energy shift and broadening of the spectra of electrons backscattered elastically from solid surfaces. *Surface and Interface Analysis*, Wiley-Blackwell, v. 31, n. 11, p. 1019–1026, oct 2001. Available at: <http://dx.doi.org/10.1002/sia.1121>. Referenced on page 33.

79 WERNER, W. S. et al. Elastic electron reflection for determination of the inelastic mean free path of medium energy electrons in 24 elemental solids for energies between 50 and 3400 eV. *Journal of Electron Spectroscopy and Related Phenomena*, Elsevier BV, v. 113, n. 2-3, p. 127–135, feb 2001. Available at: <http://dx.doi.org/10.1016/S0368-2048(00)00280-2>. Referenced on page 33.

80 WATSON, G. I. Neutron compton scattering. *Journal of Physics: Condensed Matter*, IOP Publishing, v. 8, n. 33, p. 5955–5975, aug 1996. Available at: <http://dx.doi.org/10.1088/0953-8984/8/33/005>. Referenced on page 33.

81 PAOLI, M. P.; HOLT, R. S. Anisotropy in the atomic momentum distribution of pyrolytic graphite. *J. Phys. C: Solid State Phys.*, IOP Publishing, v. 21, n. 19, p. 3633–3639, jul 1988. Available at: <http://dx.doi.org/10.1088/0022-3719/21/19/015>. Referenced on page 34.

82 PLACZEK, G. The scattering of neutrons by systems of heavy nuclei. *Phys. Rev.*, American Physical Society (APS), v. 86, n. 3, p. 377–388, may 1952. Available at: <http://dx.doi.org/10.1103/physrev.86.377>. Referenced on page 34.

83 HOVE, L. V. Correlations in space and time and born approximation scattering in systems of interacting particles. *Phys. Rev.*, American Physical Society (APS), v. 95, n. 1, p. 249–262, jul 1954. Available at: <http://dx.doi.org/10.1103/PhysRev.95.249>. Referenced on page 35.

84 VOS, M. et al. Elastic electron scattering cross sections at high momentum transfer. *Nuclear Instruments and Methods in Physics Research Section B: Beam Interactions with Materials and Atoms*, Elsevier BV, v. 300, p. 62–67, apr 2013. Available at: <http://dx.doi.org/10.1016/j.nimb.2013.01.043>. Referenced on page 35.

85 SALVAT, F.; JABLONSKI, A.; POWELL, C. J. elsepa—dirac partial-wave calculation of elastic scattering of electrons and positrons by atoms, positive ions and molecules. *Computer Physics Communications*, Elsevier BV, v. 165, n. 2, p. 157–190, jan 2005. Available at: <http://dx.doi.org/10.1016/j.cpc.2004.09.006>. Referenced on page 35.

86 CHEN, S.; MCEACHRAN, R. P.; STAUFFER, A. D. Ab initio optical potentials for elastic electron and positron scattering from the heavy noble gases. *J. Phys. B: At. Mol. Opt. Phys.*, IOP Publishing, v. 41, n. 2, p. 025201, jan 2008. Available at: <http://dx.doi.org/10.1088/0953-4075/41/2/025201>. Referenced on page 35.

87 MARMITT, G. et al. Analysis of multi-layer {ERBS} spectra. *Journal of Electron Spectroscopy and Related Phenomena*, Elsevier BV, v. 202, p. 26 – 32, jul 2015. ISSN 0368-2048. Available at: <http://www.sciencedirect.com/science/article/pii/S0368204815000419>. Referenced on page 37.

88 VOS, M. et al. Determining the band gap and mean kinetic energy of atoms from reflection electron energy loss spectra. *The Journal of Chemical Physics*, AIP Publishing, v. 143, n. 10, p. 104203, sep 2015. Available at: <http://dx.doi.org/10.1063/1.4929911>. Referenced on page 39.

89 VOS, M.; MARMITT, G. G.; GRANDE, P. L. A comparison of ERBS spectra of compounds with Monte Carlo simulations. *Surface and Interface Analysis*, Wiley-Blackwell, p. n/a–n/a, 2016. Available at: <http://dx.doi.org/10.1002/sia.5948>. Referenced on page 42.

90 MARMITT, G. et al. Oxygen diffusion in tio2 films studied by electron and ion rutherford backscattering. *Thin Solid Films*, v. 629, n. Supplement C, p. 97 – 102, 2017. ISSN 0040-6090. Available at: <http://www.sciencedirect.com/science/article/pii/S0040609017301992>. Referenced on page 46.

APPENDIX A – PowerInteraction

Here we report the development of a Monte Carlo algorithm for simulations of electron and ion beam interaction with matter. Its main feature is the use of 3D voxel matrices, where complex nanostructures or distributions of nanoparticles are comprehensively described. Thus, the algorithms involve three-dimensional 3D-spatial integration and determine the incoming- and outgoing-projectile paths numerically from the incident and scattering angles. In order to consider multiple-scattering effects, a connection trajectory algorithm was also implemented.

The PowerInteraction software was also made available for worldwide use through a web interface. The website main page is shown in Fig. 13, and may be accessed though the link <tars.if.ufrgs.br>. Powered by the TARS server, the service has attracted more than 10000 page views during the 2 years it has been online. The main server is hosted in the *Instituto de Física* of the *Universidade Federal do Rio Grande do Sul* (IF-UFRGS).

A.1 Monte Carlo simulation

The requirement for detection of an ion in a RBS experiment is that the incoming projectile has to interact with a target atom in such a way to be backscattered at the detector angle. The probability for such event is very low – as an example, for 2 MeV H^+

Figure 13 – PowerInteraction Server main webpage

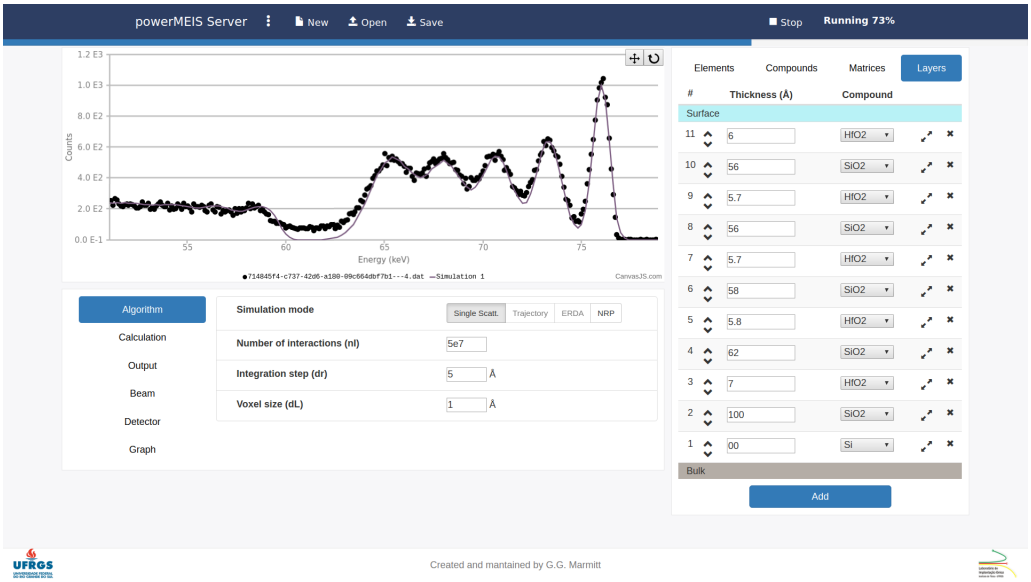

Source: Own authorship.

Figure 14 – Monte Carlo simulation

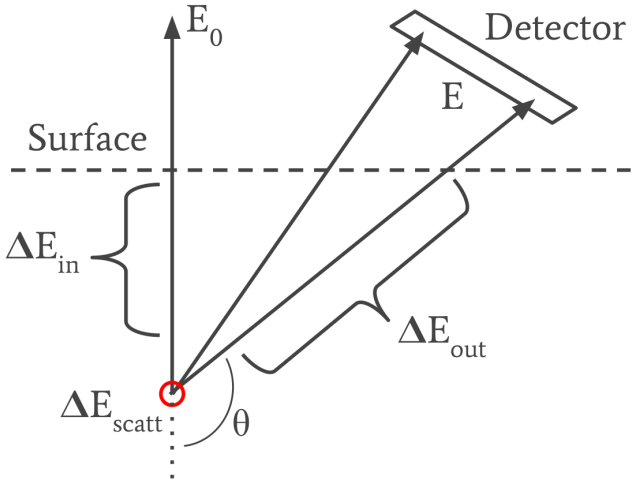

Source: Own authorship.

impinging on a 100 nm Silicon film the probability for scattering at an angle of $165 \pm 1°$ is expected to be smaller than 0.0000001%. This imposes some difficulties on the simulation of backscattering events, due to the impracticality of wasting billions of trajectories to yield one single count. In order to improve the simulation speed, PowerInteraction utilizes a Monte Carlo algorithm that only considers the cases where particles *did* interact with some target atom.

Instead of following the particle expecting it to scatter at the precise detector angle, we assume some particles will interact under those conditions. Hence, the simulation of each event first start with randomly selecting the scattering position inside the sample. Then, straight trajectories are created from the scattering point toward the surface on both the incoming and the outgoing directions, as depicted on Fig. 14. After the trajectories are known, a path integral calculates the energy loss ΔE_{in} from the surface (beam energy E_0) up to the scattering point. The elastic energy loss ΔE_{scatt} is evaluated by the kinematic factor $K_i(\theta)$, for scattering at the ith element with angle θ. Finally, the energy loss for the outgoing trajectory ΔE_{out} is calculated.

The event created must be weighted to correct for the assumption made on its inception; the very low scattering probability must be explicitly applied to build the simulation histogram. For some incident ion fluence Q, the particles detected with energy E inside a solid angle Ω may be written as a differential histogram:

$$dH_{ij}(E) = N_{ij}\ Q\ \Omega\ \sigma_i(E_1, \theta)\ f(E - E_{out})\ F^+(E)\ dEdV, \tag{A.1}$$

$$E_1 = E_0 - \Delta E_{in}, \tag{A.2}$$

$$E_{out} = K_i(\theta)E_1 - \Delta E_{out}. \tag{A.3}$$

The differential scattering cross section $\sigma_i(E_1, \Theta)$, is obtained here by solving the orbit equation using the Ziegler-Biersack-Littmark interatomic potential. The neutralization probability correction $F^+(E)$ is determined from the Marion and Young data. The energy-loss distribution $f(E-E_{out})$ is due to all energy-loss fluctuations arising from the interaction with target atoms and detection system. In the RBS technique, a Gaussian distribution has been used for $f(E - E_{out})$ because of the large number of inelastic interactions that cannot be resolved by the detection system of the technique. Here we use the Exponential Modified Gaussian (EMG) distribution for $f(E - E_{out})$, which is a simple analytic formula obtained by the convolution of a Gaussian distribution with an exponential distribution that represents the inelastic energy loss due to ionization and excitation of the backscattering atom. The energy-loss distribution f reads

$$f(\Delta E) = \alpha \exp(-\alpha \Delta E)\ \Theta(\Delta E)\ *\ \frac{1}{\sigma\sqrt{2\pi}} \exp(-\frac{\Delta E^2}{2\sigma^2}), \tag{A.4}$$

where Θ is the Heaviside step function, σ is the Gaussian straggling, and $\alpha^{-1} = \sigma_0$ is the standard deviation for the electronic energy-loss distribution in a single collision with impact parameter $b \approx 0$. The f distribution described by Eq. A.4 can be shifted by to set the mean energy loss to zero. In addition, for $\alpha\sigma \gg 1$, the EMG approaches to a Gaussian function.

The resultant spectrum $H(E)$ is obtained by integrating the Eq. A.1 over all the sample volume and adding the contribution of all elements. This method allows for simulations of any nanostructure, only requiring it to be modeled as a 3D voxel matrix.

A.2 Connected trajectories

An incoming projectile going through a material may repeatedly scatter from atoms therein, changing its energy and direction each time. For most experimental configurations these multiple collisions are not important, and may be omitted. However, for some systems such as heavy ions at low energies, the Single Scattering (SS) approximation is not enough and a Multiple Scattering (MS) simulation must be used (see Fig. 15).

One way to simulate MS is to start from outside the sample and only accept trajectories that after many collisions leave the sample's surface in the detector direction. As discussed on the last section, this *Direct Trajectory* method demands great computational effort due to its wastefulness – only a small fraction of the simulated trajectories are counted as events. Here a *Connected Trajectories* approach was used: many trajectories are constructed and then later connected and weighted. A schematic of the two algorithms is presented in Fig. (16).

In order to simulate these effects quickly, one must first create and store as many incoming and outgoing trajectories as possible – constrained by the available computer

Figure 15 – Single and multiple scattering

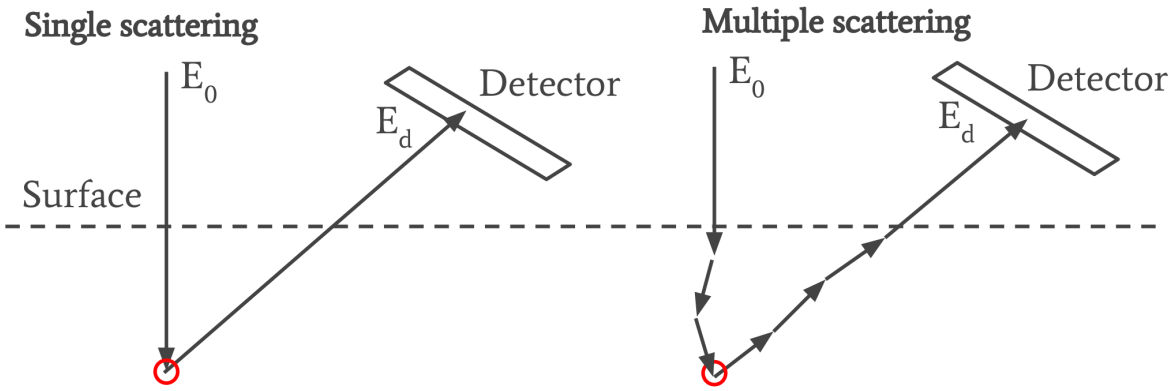

Source: Own authorship.

RAM. At a following step, trajectory pairs are connected and weighted to sum this event contribution.

Incoming and outgoing trajectories are constructed by starting with projectile following the beam and detector directions, respectively. The position, energy and path traveled by the particle are stored in each voxel it crosses during a trajectory. This data set forms a large collection of histories, some of which are incoming and some outgoing, at each matrix point. The total number of stored histories at each voxel is given by the parameter $nIon$, settable in the configuration file.

Each trajectory is constructed as follows. First, a random position (floats x, y and z) on the sample surface is chosen. In this position the incoming projectile will hit the sample's surface with the initial beam energy E_0, and from there will travel inside the material in integration steps $\vec{v} = \hat{v}dr$. The step length dr is fixed and the initial direction is the beam direction.

After each integration step, a test is performed to evaluate if an elastic collision occurred. For this, the probability of a collision with an atom during the step is needed. From the elastic scattering cross section $\sigma_i(\theta)$ of a particular element i:

$$\sigma_i^{tot} = \int_0^{\pi} \int_0^{2\pi} \sigma_i(\theta) \sin(\theta) d\alpha d\theta. \tag{A.5}$$

The total elastic scattering cross section σ_j^{tot} for a particular compound j takes into consideration the atomic fraction $f_{i,j}$ of each element in the compound,

$$\sigma_j^{tot} = \sum_i \sigma_i^{tot} f_{i,j}. \tag{A.6}$$

Taking N_j as the number of atoms per Å^3, the collision probability for each

Figure 16 – Direct and connected algorithm

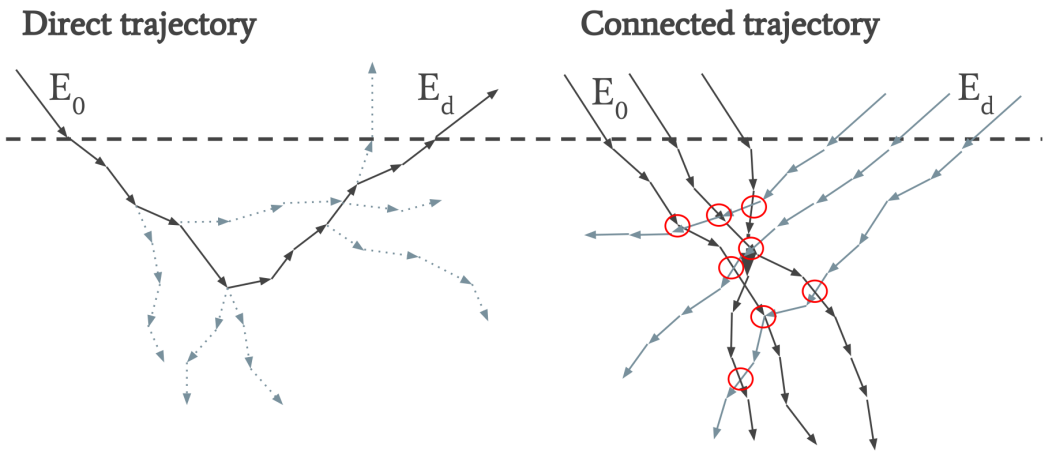

Source: Own authorship.

compound is given by:

$$P_j = \sigma_j^{tot} N_j dr. \tag{A.7}$$

If a collision occurred, i.e. $randF() < P_j$, then an element is selected as a target for the projectile to scatter. This is achieved by choosing a random number from 0 to σ_j^{tot} then accumulating σ_i^{tot} of each element.

After filling the matrix with incoming and outgoing trajectories, connections are created by randomly selecting pairs of saved stories. After choosing the pair, the scattering angle θ that connects them must be treated with some caution. If the angle is too small the scattering cross section for this connection may become very large, which lead to instabilities. To avoid such problems, we define a minimum angle θ_c from which a scattering is considered to have happened. The scattering cross section weights each connection contribution, thus integrating the differential Cross Section by Monte Carlo. Summarizing the two branches:

- If $\theta < \theta_c$ the no-collision probability is added by weighing this event contribution

$$P(\theta) = 1 - \sigma_j^{tot}; \tag{A.8}$$

- If $\theta > \theta_c$ the connection is weighted by its differential collision probability

$$P(\theta) = N_j \frac{d\sigma_i}{d\omega}(\theta)\Delta\omega dr. \tag{A.9}$$

A.3 Software implementation

In order to provide an organized framework for simulation in a diverse range of techniques and experimental configurations, PowerInteraction was coded following

Figure 17 – PowerInteraction architecture

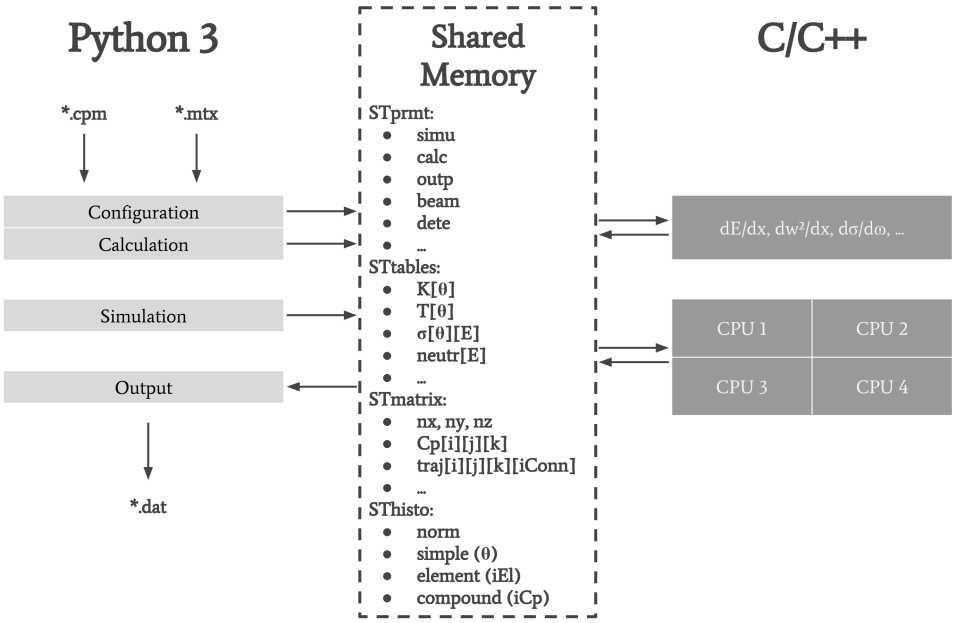

Source: Own authorship.

an architecture that is composed of an interface, support modules and a simulation kernel. The interface is a Python 3 script, which implements the basic functions such as read configuration files, allocate memory for the data structures, launch simulation threads and write output spectrum files. Support modules are written in C/C++, and are dedicated to a variety of specific tasks such as calculations of physical quantities (energy stopping/straggling, cross sections) and decompression of matrix files into voxel structures. The kernel is written in C++, and its sole duty is to run the simulations once all parameters are provided. A scheme of the PowerInteraction architecture is shown in Fig. 17.

Since the Python script may launch several simulation threads at the same time, the use of Shared Memory structures is essential. These structures are used to store all the necessary parameters (`STprmt`), calculated physical properties (`STtables`), sample's voxel matrix (`STmatrix`) and the output histogram (`SThisto`). This information is then shared between all available simulation threads (CPUs), and their progress is obtained in real time by another Python thread that periodically probes `SThisto` for new data. A Python 3 library called `ctypes` is responsible for the C memory allocation and libraries handling.

There are a number of parameters that are necessary to start a simulation, which comprise the sample structure, experimental configuration and varied simulation options. The sample is described as a series of layers, these may be composed by some chemical compounds (e.g. SiO_2), which are also described in term of their elements (e.g. Si, O).

The experimental configuration sections require information about the particle beam, the detector type and geometry. These parameters are organized in a configuration file that follows the INI file convention and are identified with a *.cpm* extension.

The configuration file is separated into several sections. The first sections define simulation parameters and select which physical models to use during calculations:

- `[simulation]` - Monte Carlo parameters
  - `algorithm` - single scattering (`ssct`), connected trajectories (`traj`)
  - `nI` - number of Monte Carlo events
  - `dL` - lateral size of each cubic voxel, in Å
  - `dr` - simulation step, in Å
  - `cores` - select the number of processors cores to be used, enables multithreading
  - `line shape` - select an energy loss function; `gauss` or `EMG`
  - `cross section` - select between classical (`Rutherford`) and screening corrected (`correc`)
- `[calculation]` - physical models
  - `stopping` - energy stopping calculation; only supports SRIM's `stop96`
  - `straggling` - energy straggling calculation; choose among `Bohr`, `Lind`, `Chu` and `Yang`
  - `neutralization` - ion neutralization model; options are `off`, `Marion` and `CasP`
- `[coulomb explosion]` - used with molecular beams
  - `ratio` - energy stopping ratio, only applied to the incoming particles
  - `gamma` - linear parameter γ of the coulomb explosion model
  - `alpha` - saturation parameter α of the coulomb explosion model
- `[trajectory]` - connected trajectory options
  - `MS` - enable/disable multiple scattering, boolean (yes/no)
  - `max distance` - maximum distance traveled by the particle, in Å
  - `angle min` - minimum angle accepted for a connection, in degrees (°)
  - `accept dE` - maximum difference in energy between incoming and outgoing trajectories accepted for a connection, in keV
  - `memory` - available RAM to store trajectory data, in MBs
- `[output]` - output spectrum parameters
  - `histogram` - histogram type; options are energy/angle (`simple`), energy/element (`element`) and energy/compound (`compound`)
  - `Emin` - initial value in energy window
  - `Emax` - final value in energy window
  - `dEnergy` - energy step in energy window

  - `dAngle` - angle step in angle window, if applicable

Next comes the experimental description, divided in two sections:

- `[beam]` - beam particles
  - `type` - particle type, options are `ion`, `molecule` and `electron`
  - `Z` - atomic number
  - `M` - atomic mass, in a.m.u.
  - `E0` - particle energy, in keV
  - `theta inc` - incoming angle in relation with the sample normal, in degrees (°)
- `[detector]` - detector type and geometry
  - `type` - detector type, options are `electro`, `magnetic` and `TOF`
  - `resolution` - experimental energy resolution, peak FWHM in eV
  - `Y0` - scattering angle of the detector center, in degrees (°)
  - `LY` - angular width of the detector, in degrees (°)
  - `X0` - out of plane angle of the detector center, in degrees (°)
  - `LX` - angular width of the detector in the out of plane direction, in degrees (°)
  - For Time of Flight detectors (TOF)
    - `TOF resolution` - detector time resolution, peak FWHM in ns
    - `TOF distance` - distance between the sample and detector, in m

The sample description require information of elements, compounds and layers:

- `[elements]` - elements used to make up compounds
  - `name` - internal element name
  - `Z` - atomic number
  - `M` - atomic mass, in a.m.u.
  - `sig0` - exponential factor σ_0 in the EMG, in eV
- `[compounds]` - compounds that constitute layers
  - `name` - internal compound name
  - `density` - compound density, in g/cm^3
  - `%element X` - element stoichiometry in the compound
- `[layers]` - layers used to describe the sample
  - Film parameters
    - `thickness` - film thickness, in Å
    - `compound` - index of the compound that constitutes this layer
  - Nanostructure parameters
    - `file` - File name of the matrix

* `periodic contourn` - used for periodic countourn boundaries condition, boolean (yes/no)
* `periodic position` - used for aligned periodic samples, boolean (yes/no)

A.4 Modeling nanostructures

One of the great advantages of the program PowerInteraction is its capability to simulate any nanostructure. However, in order to do so the user has to provide a full 3D matrix, for each nanostructure of the sample, which are then read by PowerInteraction. The nanostructures are divided into voxels with volume dV. These are small 3D cells, each containing an index representing some chemical composition with determined density, stopping power, straggling and stoichiometry. The matrix is build layer-by-layer, from top (surface) to bottom (bulk). For the case of a spherical nanoparticle on top of a surface, an example illustrating each layer of the matrix is shown in Fig. 18.

The PowerInteraction software does not generate the matrix files. The matrices can be generated either by hand (in the text file) or by another program (especially created by the user) by using an algorithm capable to create the matrix that best represents the desired nanostructure model. A single matrix can represent from a simple spherical nanoparticle up to a more complex structures, constituted by several hundred particles with distinct size and geometries. In practice, there is no other limit to the matrix size than the computer memory.

The matrix representing a nanostructure is stored in a matrix file *.mtx*, that contains a compressed representation of the matrix. For each matrix, represented like in Fig. 18, the compression is performed by counting the number of repetitions of adjacent compositions. Then for the first composition, a combination of *repetitions compound* is stored and the next composition is counted. The matrix file format should be formatted as a text file:

```
nx ny nz phi
r1 c1
r2 c2
r3 c3
...
```

Where: `nx`, `ny`, `nz` are the matrix dimension size in the x, y and z directions; `phi` is the rotation around the z axis (in degrees); and `ri` is the number of repetitions of a correspondent index `ci` of the sequence `i`.

A simple visualizer for matrix files is available online on the PowerInteraction platform, showed in Fig. 19. It has support for matrices in *.mtx* (PowerInteraction) and *.prf* (TRI3DYN) formats, with support for 1000+ compounds.

Figure 18 – Voxel matrix file

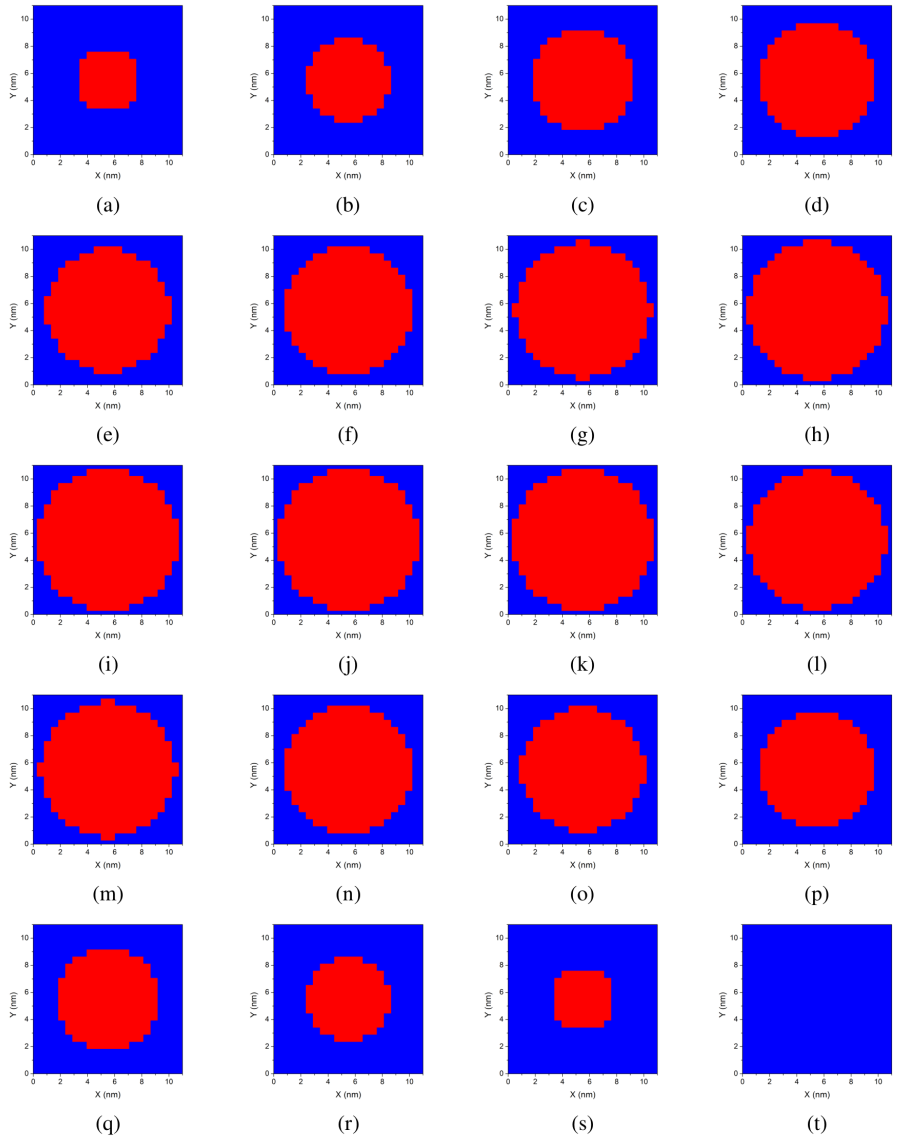

Source: Own authorship.

Note: Example on how to construct a matrix that represents a spherical nanoparticle of some chemical composition (red clusters) of radius equal to 5 nm. The edge of the cluster is 0.5 nm. Each figure, from bottom (a) to top (t), represents layers of 0.5 nm thickness. The blue clusters can represent another chemical composition (or just vacuum).

A.5 TARS Server

Monte Carlo algorithms have several advantages when compared to analytic approaches, but they can be very computationally expensive. One solution for low power devices is the use of centralized servers, where all the hard work is taken care of. Thus, following a modern trend, we have developed a cloud computing platform for the simulation

Figure 19 – Matrices of voxels representing 3D Nanostructures

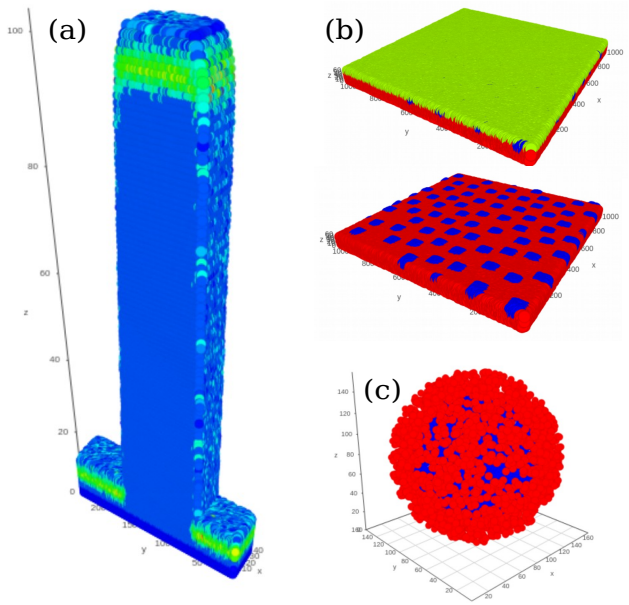

Source: Own authorship.

Note: In (a), a segment of 200 nm Si trenches generated by a TRI3DYN implantation simulation; in (b), a group of Au nanoparticles in the Si/SiO 2 interface [2]; in (c), a Pt/Pd coreshell with 14 nm diameter.

of MEIS/RBS spectra. The PowerInteraction software was integrated into a web server, which provides for users worldwide the possibility to make simulations and analyze spectra through any modern web browser.

The server architecture (see Fig. 20) is composed of three main sections: the website, the server manager, and the simulation workers. The website was developed using the Bootstrap (<getbootstrap.com>) environment, both for its CSS styling and HTML facilities. Heavy use of JavaScript (JS) was made, through the nice HTML/JS interface provided by AngularJS (<angularjs.org>). For the interactive graph plotting, the Plotly (<plot.ly>) library was used. The real time communication between the client and server is made through the `EventSource` API, where the client repeatedly asks for updated data being processed on the server. The server manager is written in Python 3, and its function is to receive, process and deliver requests from clients. Once a request for new simulation is made, the manager creates a new `Worker` instance. The `Worker` runs simulations as separated processes, and is linked via the `pipe` API to its correspondent `Job` object in the server manager process.

The server runs asynchronously, handling simultaneous simulations for multiple

Figure 20 – Server architecture

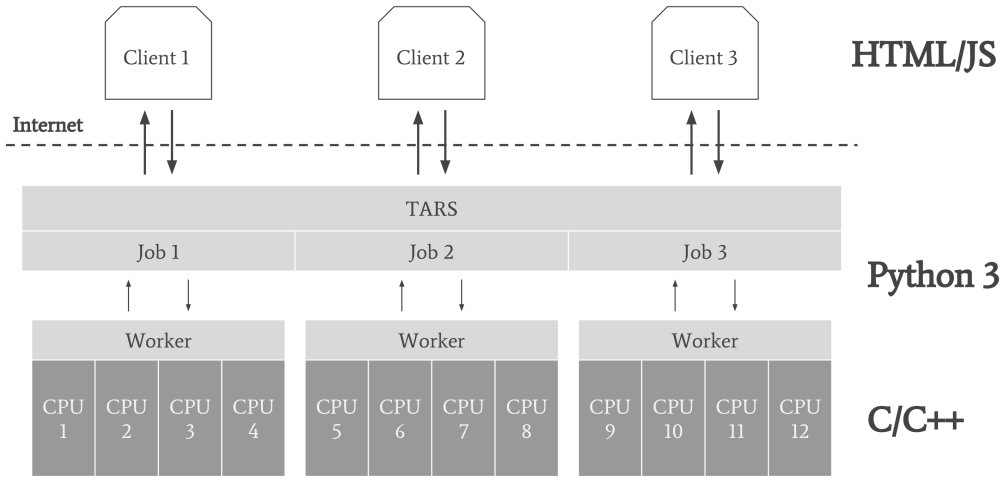

Source: Own authorship.

users at the same time. This platform was extensively used for all MEIS spectra fittings during the 2nd Round Robin Table for MEIS. Hosted on the IF-UFRGS's computer cluster, the TARS server specs are:

- Intel Core i7-5930K with 12 cores at 3.5GHz;
- Gigabyte GA-X99-UD3;
- 32GB DDR4 2133MHz;
- Debian Linux;
- 100 Mb/s internet connection.